Cyclic nucleotide-induced helical structure activates a TIR immune effector

Gaëlle Hogrel[1], Abbie Guild[2,3], Shirley Graham[1], Hannah Rickman[1], Sabine Grüschow[1], Quentin Bertrand[4,a], Laura Spagnolo[2*] and Malcolm F White[1*]

[1] University of St Andrews, School of Biology, North Haugh, St Andrews KY16 9TZ; [2] University of Glasgow, Institute of Molecular, Cell and Systems Biology, Garscube Campus, Glasgow G61 1QH; [3] Centre for Regenerative Medicine, Institute for Regeneration and Repair, The University of Edinburgh, Edinburgh BioQuarter, 5 Little France Drive, Edinburgh EH16 4UU; [4] Univ. Grenoble Alpes, CNRS, CEA, IBS, Grenoble, France.

[a]Present address: Laboratory of Biomolecular Research, Biology and Chemistry Division, Paul Scherrer Institute, Villigen, Switzerland.

* for correspondence email mfw2@st-andrews.ac.uk; Laura.Spagnolo@glasgow.ac.uk

Cyclic nucleotide signalling is a key component of anti-viral defence in all domains of life. Viral detection activates a nucleotide cyclase to generate a second messenger, resulting in activation of effector proteins. This is exemplified by the metazoan cGAS-STING innate immunity pathway [1], which originated in bacteria [2]. These defence systems require a sensor domain to bind the cyclic nucleotide and are often coupled with an effector domain that causes cell death when activated by destroying essential biomolecules [3]. One example is the TIR (Toll/interleukin-1 receptor) domain, which degrades the essential cofactor NAD^+ when activated in response to infection in plants and bacteria [2,4,5] or during programmed nerve cell death [6]. Here, we show that a bacterial anti-viral defence system generates a cyclic tri-adenylate (cA_3) which binds to a TIR-SAVED effector, acting as the "glue" to allow assembly of an extended superhelical solenoid structure. Adjacent TIR subunits interact to organise and complete a composite active site, allowing NAD^+ degradation. Activation requires extended filament formation, both *in vitro* and *in vivo*. Our study illuminates a striking example of large-scale molecular assembly controlled by cyclic nucleotides and reveals key details of the mechanism of TIR enzyme activation.

Cyclic nucleotide second messengers play a central role in prokaryotic anti-viral defence by type III CRISPR [7,8], CBASS (Cyclic nucleotide Based Antiphage Signalling Systems) [3] and PYCSAR (Pyrimidine Cyclase System for Antiphage Resistance) [9]. These systems activate potent effector proteins that destroy key cellular components such as nucleic acids, cofactors or membranes to disrupt viral replication [3,10]. A good example is the TIR domain, which functions as an enzyme that degrades NAD^+ to cause cell death in plants infected with pathogens [5,11], anti-phage immunity in the bacterial Thoeris [12,13] and TIR-STING [2] systems, and programmed nerve cell death in metazoa [6]. TIR domain activation requires effector subunit assembly, but the molecular mechanisms are still not fully understood.

cA_3 activates TIR-SAVED to degrade NAD^+

Type III CRISPR and CBASS systems both use the SAVED (SMODS-associated and fused to various effector domains) cyclic nucleotide binding sensor domain [14,15]. Here we focussed on a Type II-C CBASS from the Gram-positive bacterium *Microbacterium ketosireducens* (Mke) [16] which has a nucleotide cyclase (CD-NTase), TIR-SAVED and NucC effectors, along with an ubiquitin-like modification system of unknown function (Fig. 1a). We designed synthetic genes for the expression of the CD-NTase and TIR-SAVED proteins in *E. coli* and purified the recombinant proteins using cleavable N-terminal his-tags and gel filtration (Supplemental Data Fig. 2). We investigated the activity of the cyclase by incubating the protein with a range of nucleotides, including α-^{32}P-ATP for visualisation, and analysis by thin layer chromatography (TLC). A radioactive product running at the position of a cA_3 standard was observed when ATP was present in the reaction (Fig. 1b), and the addition of other nucleotides did not result in any observable change (Extended Data Fig.1a). The analysis of the reaction products by liquid chromatography confirmed that the cyclase uses ATP to produce cA_3 that co-elutes with a synthetic 3',3',3'-cA_3 standard (Fig. 1c).

To investigate the activity of the TIR-SAVED effector, we used ε-NAD^+, an NAD analogue that emits a fluorescent signal on cleavage by TIR proteins (Fig. 1d) [2,11]. We screened a range of commercially available cyclic nucleotide molecules for the ability to activate the TIR-SAVED effector, observing that only cA_3 resulted in generation of a fluorescent signal (Extended Data Fig. 1b). We proceeded to couple the cyclic nucleotide production by the cyclase with the NADase assay to follow the activation of TIR-SAVED. In the presence of ATP the cyclase activated the TIR-SAVED effector to degrade NAD^+ (Fig. 1e). Together these data demonstrate that the CD-NTase synthesises a 3',3',3'-cA_3 product that can activate the TIR-SAVED NADase activity.

The initial rate of NAD^+ cleavage increased linearly with cA_3 concentration up to a value of 0.5 μM cA_3, which corresponded with the concentration of TIR-SAVED in the assay, consistent with a 1:1 molar ratio of cA_3 to TIR-SAVED in the activated form of the effector (Extended Data Fig. 1c). We next examined the Michaelis-Menten parameters of TIR-SAVED NADase activity, determining a K_M of 470 μM and a k_{cat}/K_M of 2.08 x 10^3 $M^{-1}s^{-1}$ (Extended Data Fig. 1d). This K_M value fits in the concentration range of NAD^+ found in mammalian cells and *E. coli* (200-640 μM) [17,18]. Various bacterial TIR proteins have estimated K_M values between 196 and 488 μM [4]. In the *Thoeris* system of *Bacillus cereus*, the NADase enzyme ThsA activated by cyclic ADP ribose (cADPr) has a K_M of 270 μM for NAD and a catalytic efficiency (k_{cat}/K_M) of 2.1 x 10^3 $M^{-1}s^{-1}$ [13], in good agreement with our observations.

Activation of TIR-SAVED kills cells

CBASS defence systems tend to be phage and host species specific, and the mechanism of activation in response to phage infection remains largely unknown [19]. As we could not analyse CBASS activity in the cognate host, we took advantage of the observation that TIR-SAVED is activated by cA_3 by coupling the effector with a type III CRISPR system from *Mycobacterium tuberculosis (Mtb)*, which generates a range of cyclic oligoadenylate species including cA_3 on detection of target RNA [20]. Here, we replaced the cognate Csm6 effector with Mke TIR-SAVED and programmed the CRISPR system with a guide RNA complementary to the tetracycline resistance gene *tetR* (Fig. 1f, Extended Data Fig. 2). When the active CRISPR system was present along with wild-type TIR-SAVED, transformation of a target plasmid containing the *tetR* gene resulted in no cell growth on plates containing tetracycline (Fig. 1g). This phenotype required the production of cA_3 (Extended Data Fig. 2) and the NADase activity of TIR-SAVED, as variant E84Q, which targets the active site (Fig. 1g), relieved the effect [2,11,12]. This suggests that TIR-SAVED, activated by cA_3, is responsible for cell death by NAD^+ hydrolysis.

Structure of the TIR-SAVED complex

The structure of the TIR-SAVED monomer was predicted using Alphafold2 (AF2) [21] as implemented by the Colabfold server [22] (Supplemental Data Fig. 3). Size exclusion chromatography (SEC) combined with Small-Angle X-ray scattering (SAXS) indicated that TIR-SAVED tends to be monomeric in solution (Extended Data Fig. 3a,b). However, addition of cA_3 to the protein resulted in a significant increase in global particle size by Dynamic Light Scattering (Fig. 2a) and a dramatic shift in the elution volume on SEC (Extended data Fig. 3c), suggesting the presence of high molecular weight complexes. These data strongly suggest that cA_3 binding induces multimerization of the TIR-SAVED protein, reminiscent of that observed for the SAVED domain-containing Cap4 protein, where head-to-tail multimers of two or three subunits were observed by electron microscopy [23].

Cryo-electron microscopy demonstrated that cA_3 drove the formation of ordered TIR-SAVED filaments (Fig. 2b). The assembly is characterised by a right-handed superhelical solenoid with 22 nm diameter and a 14 nm pitch. 17 TIR-SAVED monomers are present in each turn of the filament (Fig. 2b). Local resolution analysis performed with the CryoSPARC package highlighted a slightly anisotropic resolution, going from 2.5 to 5 Å (Extended data Fig. 4). 3D variability analysis of a structure including two turns of the solenoid highlighted a degree of flexibility over the filament (Supplemental Data Fig. 5, 6 and supplementary videos 1-6). The variability analysis shows a slight variation in the radius of the filaments, as well as in its pitch, therefore we chose to proceed with the cryo-EM reconstruction of one turn of the complex in

isolation, and with the fitting of the four higher resolution protomers, which provides information on protein/protein and protein/ligand interface.

To build a model of TIR-SAVED, we used four copies of the AF2 output as a starting model for rigid body fitting using Chimera and the rigid-body fitted tetramer was then refined as described in the methods (Fig. 2c; Extended data Fig. 4f, 5). Four densities that correspond to the characteristic shape and size of the cA_3 ligand [23], visible in the outstanding density, were fitted and refined (Fig. 2d). The final atomic model confirmed the head-to-tail assembly where the cA_3 was located in the SAVED domain binding pocket of subunit 1, interacting with conserved residues including W394 and K199. The binding site is completed by interactions with subunit 2, including conserved residue R388 (Fig. 2e), resulting in "sandwiching" of cA_3 between the two SAVED domains (Supplemental video 7). The SAVED domain is a distant cousin of the cOA-sensing CARF domain associated with type III CRISPR systems [15], and is found in 30% of CBASS operons [23]. SAVED domains fused to nucleases bind cyclic di- and tri-nucleotides, activating the associated nuclease domain for DNA degradation [23,24]. Our data suggest that head-to-tail stacking of SAVED domains, potentiated by cyclic nucleotide binding, is a defining feature of effector activation.

Generation of a composite active site

TIR domains are ubiquitous, performing both protein scaffolding and enzymatic roles in different contexts across all three domains of life (reviewed in [4]). As is the case for TIR-SAVED, the catalytically active TIR domains, which degrade NAD^+ to cause cell death, typically rely on multimerization linked to activation [2,4,5,11,25,26], but the molecular mechanism for this activation is not well understood. In the filament assembly, TIR domains display a conserved interaction interface involving the BB loop (Extended Data Fig. 6) of subunit 1, which is held in a configuration that exposes the active site, due to interaction with the DE loop from the adjacent subunit (Fig. 2f). This BB-loop interface is also observed in TIR proto-filament formation such as for the catalytically inactive TIR domain of the human MAL Toll-like receptor protein [27] and the active from of human SARM1 [28]. The BB loop is suspected, in other NAD^+ consuming TIR proteins, to regulate the access to the active site [11,29 25,26] and it has been proposed recently for the RUN1-TIR domain that the DE loop of the adjacent subunit contributes to NAD binding [29].

We therefore tested the hypothesis that a composite NADase active site is formed at the interface between two adjacent TIR domains in the TIR-SAVED filament (Fig. 2f). We first investigated the BB loop, showing that a variant protein with the double mutation D45A/L46A completely lacked NADase activity (Fig. 2g) without affecting cA_3-dependent multimerization (Extended Data, Fig. 7a). We proceeded to explore the role of putative NAD^+ binding site by

mutating the highly conserved residue Tyr-115 in the DE loop, which is suitably positioned to interact with NAD^+ in the TIR-SAVED filament (Fig. 2f). The Y115A variant had only 10 % of the NADase activity of the wild-type enzyme, together with a 3-fold increase in K_M for εNAD^+, suggesting a direct role in the catalytic cycle rather than just substrate binding (Fig. 2g, Extended Data, Fig. 7b, c). This supports the model of a composite NADase active site that has also been proposed for the TIR-NLR RPP1 immune receptor [26] and SARM1 [28], and is likely to be broadly relevant for catalytic TIR proteins.

Filamentation is essential for activation

The composite active site of TIR-SAVED requires adjacent TIR domains to be brought together during the activation process. Nevertheless, it does not necessarily follow that the extended helical conformation of the effector observed here is relevant for function, as it could be an *in vitro* artifact of the assembly. To investigate this, three different site directed variants were generated and assayed (Fig. 3a). TIR-SAVED variant E (E84Q), which knocks out the TIR active site, can multimerise but lacks NADase activity (Extended Data, Fig. 8). Variant R (R388E), which reverses the charge of a conserved residue contributed by subunit 2 in the cA_3 interface (Fig. 2e), retained the ability to bind cA_3 but was unable to multimerise and was catalytically inactive (Fig. 3b, Extended Data, Fig. 8). Finally, we generated variant KW (K199E/W394A), targeting two conserved residues in the cA_3 binding site of subunit 1 (Fig. 2e). This variant no longer bound cA_3 and remained monomeric (Fig. 3b, Extended Data Fig. 8b).

Although each of these variants was inactive in isolation, they could be combined to generate further variations of the TIR-SAVED complex in a defined manner. Firstly, we investigated the combination of the R and KW variants. Each has one wild-type and one compromised cA_3 binding surface, and they can be combined along with cA_3 to generate a TIR-SAVED dimer with one composite active site (where the R and KW variants function as subunit 1 and 2, respectively, in Fig. 2e). The dimeric composition was confirmed by analytical gel filtration and native PAGE (Extended Data, Fig. 9a, b). Unexpectedly however, the dimer of TIR-SAVED displayed no NADase activity on addition of cA_3 (Extended Data, Fig. 9c), despite the provision of both halves of the shared active site. We therefore combined the R variant with the E variant, a combination which can result in the generation of filaments of varied size, but with only one active site as the R variant can only be extended by successive addition of inactive E variant subunits (Fig. 3a). By assaying this combination, we observed a recovery of NADase activity that increased progressively as the E variant was added. The initial activity continued to increase up to the highest ratio (1:32) of R:E studied, representing two turns of the helix on

average – indicating that longer filaments of TIR-SAVED have higher levels of NADase activity even if there is only one active site in each filament (Fig. 3c, Extended Data Fig. 9d). These observations highlight the requirement that catalytic TIR domains assemble into multimers, not just dimers, for activation.

While these observations confirmed the importance of filament assembly for TIR-SAVED activation *in vitro*, we wished to explore whether the same held true *in vivo*. To explore this, we created a second copy of the *tir-saved* gene to allow expression of combinations of variant proteins in our plasmid challenge assay. For the second copy of the gene, we used alternative codons to avoid any problems caused by recombination between two highly similar sequences in a plasmid. Using this experimental design, we tested whether the results obtained *in vitro* could be recapitulated *in vivo* (Fig. 3d). The R variant alone afforded a modest degree (1 log) of protection *in vivo*, far lower than observed for the wild-type protein. A combination of the R and KW variant genes produced a null phenotype, confirming the lack of activity observed *in vitro*. However, when the R variant was combined with the inactive E variant, a significant level of effector activity was observed in the plasmid challenge assay, confirming the requirement for filament formation observed *in vitro* (Fig. 3c, d). Thus, we conclude that extended filament formation is relevant and essential for the function of the TIR-SAVED effector.

Wider aspects of TIR domain activation

Here we have explored a CBASS system with a TIR-SAVED effector that oligomerises on activation by cA_3. Oligomerisation with "open symmetry" (the ability to polymerize to infinity) seems to be a widespread property of prokaryotic innate immune effectors, encompassing the bacterial STING, SAVED and PYCSAR proteins [2,9,23]. We have demonstrated that this oligomerisation is essential for TIR-SAVED function; firstly, as it likely allows access to the active site by formation of the BE interface, prising open the BB loop; secondly, as residues from the adjacent subunit participate in substrate binding and the catalytic cycle. Thus, the bacterial TIR-domain effectors appear to conform to the emerging paradigm of "signaling by cooperative assembly formation" (SCAF) proposed for the eukaryotic signalling complexes [30]. Interestingly, the bacterial TIR-SAVED filament displays the evolutionarily conserved head-to-tail arrangement in the TIR domain at the BE interface also found in eukaryotic TIR enzymes such as SARM1[28] and RPP1 [29] (Fig. 4) which is likely to be a prerequisite for TIR activation in all systems. However, our data demonstrate that it is not sufficient to assemble this interface, as dimeric TIR-SAVED is inactive both *in vitro* and *in vivo*. Activation requires assembly of larger complexes, which may be essential to stabilise the TIR domain in an active conformation. In RPP1 and SARM1, TIR domains form tetrameric and octameric complexes with the AE interface formed by interactions between the αA and αE helices of TIR domains,

perpendicular to the BE interface (Fig. 4). Here the TIR-SAVED assembly is unique as there is only a single filament of TIR domains, and it is notable that the SAVED domain occupies the space where the AE interface forms in the eukaryotic proteins (Fig. 4). Oligomerisation-dependent activation of bacterial TIR effectors is likely to be the ancestral mechanism underlying the whole family of catalytic and non-catalytic TIR signalling complexes, exemplified by the accompanying study of the bacterial TIR-STING effector [31]. Our study reveals that activation is tightly controlled, requiring more than two TIR-domains to be brought together. This suggests that the stabilization of the active form of TIR proteins requires extensive protein interactions, and possibly an alteration in dynamics, beyond the formation of the crucial BE interface – a property that may have evolved to avoid "accidental" activation of TIR domains and autotoxicity.

REFERENCES

1 Cai, X., Chiu, Y. H. & Chen, Z. J. The cGAS-cGAMP-STING pathway of cytosolic DNA sensing and signaling. *Mol. Cell* **54**, 289-296, doi:10.1016/j.molcel.2014.03.040 (2014).

2 Morehouse, B. R. *et al.* STING cyclic dinucleotide sensing originated in bacteria. *Nature* **586**, 429-433, doi:10.1038/s41586-020-2719-5 (2020).

3 Millman, A., Melamed, S., Amitai, G. & Sorek, R. Diversity and classification of cyclic-oligonucleotide-based anti-phage signalling systems. *Nat Microbiol* **5**, 1608-1615, doi:10.1038/s41564-020-0777-y (2020).

4 Essuman, K. *et al.* TIR Domain Proteins Are an Ancient Family of NAD(+)-Consuming Enzymes. *Curr Biol* **28**, 421-430 e424, doi:10.1016/j.cub.2017.12.024 (2018).

5 Wan, L. *et al.* TIR domains of plant immune receptors are NAD(+)-cleaving enzymes that promote cell death. *Science* **365**, 799-803, doi:10.1126/science.aax1771 (2019).

6 Summers, D. W., Gibson, D. A., DiAntonio, A. & Milbrandt, J. SARM1-specific motifs in the TIR domain enable NAD+ loss and regulate injury-induced SARM1 activation. *Proc. Natl. Acad. Sci. USA* **113**, E6271-E6280, doi:10.1073/pnas.1601506113 (2016).

7 Kazlauskiene, M., Kostiuk, G., Venclovas, C., Tamulaitis, G. & Siksnys, V. A cyclic oligonucleotide signaling pathway in type III CRISPR-Cas systems. *Science* **357**, 605-609, doi:10.1126/science.aao0100 (2017).

8 Niewoehner, O. *et al.* Type III CRISPR-Cas systems produce cyclic oligoadenylate second messengers. *Nature* **548**, 543-548, doi:10.1038/nature23467 (2017).

9 Tal, N. *et al.* Cyclic CMP and cyclic UMP mediate bacterial immunity against phages. *Cell* **184**, 5728-5739 e5716, doi:10.1016/j.cell.2021.09.031 (2021).

10 Athukoralage, J. S. & White, M. F. Cyclic oligoadenylate signalling and regulation by ring nucleases during type III CRISPR defence. *RNA* **27**, 855-867, doi:10.1261/rna.078739.121 (2021).

11 Horsefield, S. *et al.* NAD(+) cleavage activity by animal and plant TIR domains in cell death pathways. *Science* **365**, 793-799, doi:10.1126/science.aax1911 (2019).

12 Ofir, G. *et al.* Antiviral activity of bacterial TIR domains via immune signalling molecules. *Nature* **600**, 116-120, doi:10.1038/s41586-021-04098-7 (2021).

13 Ka, D., Oh, H., Park, E., Kim, J. H. & Bae, E. Structural and functional evidence of bacterial antiphage protection by Thoeris defense system via NAD(+) degradation. *Nature communications* **11**, 2816, doi:10.1038/s41467-020-16703-w (2020).

14 Burroughs, A. M., Zhang, D., Schaffer, D. E., Iyer, L. M. & Aravind, L. Comparative genomic analyses reveal a vast, novel network of nucleotide-centric systems in

biological conflicts, immunity and signaling. *Nucl. Acids Res.* **43**, 10633-10654, doi:10.1093/nar/gkv1267 (2015).
15 Makarova, K. S. *et al.* Evolutionary and functional classification of the CARF domain superfamily, key sensors in prokaryotic antivirus defense. *Nucl. Acids Res.* **48**, 8828-8847, doi:10.1093/nar/gkaa635 (2020).
16 Takeuchi, M. & Hatano, K. Proposal of six new species in the genus Microbacterium and transfer of Flavobacterium marinotypicum ZoBell and Upham to the genus Microbacterium as Microbacterium maritypicum comb. nov. *Int J Syst Bacteriol* **48 Pt 3**, 973-982, doi:10.1099/00207713-48-3-973 (1998).
17 Canto, C., Menzies, K. J. & Auwerx, J. NAD(+) Metabolism and the Control of Energy Homeostasis: A Balancing Act between Mitochondria and the Nucleus. *Cell Metab* **22**, 31-53, doi:10.1016/j.cmet.2015.05.023 (2015).
18 Zhou, Y. *et al.* Determining the extremes of the cellular NAD(H) level by using an Escherichia coli NAD(+)-auxotrophic mutant. *Appl Environ Microbiol* **77**, 6133-6140, doi:10.1128/AEM.00630-11 (2011).
19 Lowey, B. & Kranzusch, P. J. CD-NTases and nucleotide second messenger signaling. *Curr Biol* **30**, R1106-R1108, doi:10.1016/j.cub.2020.06.096 (2020).
20 Grüschow, S., Athukoralage, J. S., Graham, S., Hoogeboom, T. & White, M. F. Cyclic oligoadenylate signalling mediates Mycobacterium tuberculosis CRISPR defence. *Nucl. Acids Res.* **47**, 9259-9270, doi:https://doi.org/10.1101/667758 (2019).
21 Jumper, J. *et al.* Highly accurate protein structure prediction with AlphaFold. *Nature* **596**, 583-589, doi:10.1038/s41586-021-03819-2 (2021).
22 Mirdita, M., Ovchinnikov, S. & Steinegger, M. ColabFold - Making protein folding accessible to all. *Nat Methods* doi:10.1038/s41592-022-01488-1 (2022).
23 Lowey, B. *et al.* CBASS Immunity Uses CARF-Related Effectors to Sense 3'-5'- and 2'-5'-Linked Cyclic Oligonucleotide Signals and Protect Bacteria from Phage Infection. *Cell* **182**, 38-49 e17, doi:10.1016/j.cell.2020.05.019 (2020).
24 Fatma, S., Chakravarti, A., Zeng, X. & Huang, R. H. Molecular mechanisms of the CdnG-Cap5 antiphage defense system employing 3',2'-cGAMP as the second messenger. *Nature Commun.* **12**, 6381, doi:10.1038/s41467-021-26738-2 (2021).
25 Martin, R. *et al.* Structure of the activated ROQ1 resistosome directly recognizing the pathogen effector XopQ. *Science* **370**, doi:10.1126/science.abd9993 (2020).
26 Ma, S. *et al.* Direct pathogen-induced assembly of an NLR immune receptor complex to form a holoenzyme. *Science* **370**, doi:10.1126/science.abe3069 (2020).
27 Ve, T. *et al.* Structural basis of TIR-domain-assembly formation in MAL- and MyD88-dependent TLR4 signaling. *Nat Struct Mol Biol* **24**, 743-751, doi:10.1038/nsmb.3444 (2017).
28 Shi, Y. *et al.* Structural basis of SARM1 activation, substrate recognition, and inhibition by small molecules. *Mol. Cell*, doi:10.1016/j.molcel.2022.03.007 (2022).
29 Burdett, H., Hu, X., Rank, M. X., Maruta, N. & Kobe, B. Self-association configures the NAD⁺-binding site of plant NLR TIR domains. *bioRxiv*, 2021.2010.2002.462850, doi:10.1101/2021.10.02.462850 (2021).
30 Vajjhala, P. R., Ve, T., Bentham, A., Stacey, K. J. & Kobe, B. The molecular mechanisms of signaling by cooperative assembly formation in innate immunity pathways. *Mol Immunol* **86**, 23-37, doi:10.1016/j.molimm.2017.02.012 (2017).
31 Morehouse, B. R. *et al.* Cryo-EM structure of an active bacterial TIR-STING filament complex. *Nature*, in press (2022).
32 Grüschow, S., Adamson, C. S. & White, M. F. Specificity and sensitivity of an RNA targeting type III CRISPR complex coupled with a NucC endonuclease effector. *Nucl. Acids Res.*, gkab119, doi:10.1101/2021.09.13.460032 (2021).
33 Rouillon, C., Athukoralage, J. S., Graham, S., Grüschow, S. & White, M. F. Investigation of the cyclic oligoadenylate signalling pathway of type III CRISPR systems. *Methods Enzymol* **616**, 191-218 (2019).
34 Whiteley, A. T. *et al.* Bacterial cGAS-like enzymes synthesize diverse nucleotide signals. *Nature* **567**, 194-199, doi:10.1038/s41586-019-0953-5 (2019).

Fig.1 Mke CBASS generates a cA_3 second messenger to activate the TIR-SAVED NADase effector. a, Mke CBASS operon (RS81_contig000028). **b**, The cyclase (CD-NTase) uses ATP to produce cyclic-oligoadenylate (cOA) products (lane 3), visualised after TLC. Negative control without protein (lane 2), positive control (lane 1) cA_3 produced using the Type III CRISPR complex of *Vibrio metoecus* [32]. Gel source data in Supplemental Data Fig. 1a. **c**, HPLC analysis of reaction products confirmed the cA_3 product. Raw figure available in Supplemental Data Fig. 1b. **d**, Schematic of the reaction used to analyse TIR-SAVED NADase activity. **e**, Cyclase products activate TIR-SAVED NADase activity. The CD-NTase was incubated with ATP for 2 h before adding ε-NAD^+ and TIR-SAVED. Data are means plotted with standard deviation for triplicate experiments. **f**, Schematic of the plasmid challenge assay. The Type III CRISPR complex produces cA_3 on binding the target transcript, activating TIR-SAVED NADase activity. **g,** *E. coli* transformants after plasmid immunity assay of *Mtb*Csm (Type III CRISPR system) combined with TIR-SAVED. Wild-type TIR-SAVED prevents the growth of transformants whereas the inactive E84Q variant does not. Additional conditions, replicates and details of the constructs are shown in Extended data Fig. 2.

Fig.2 Structure of the activated TIR-SAVED/cA_3 assembly. a, Dynamic light scattering shows that TIR-SAVED increases in size on cA_3 binding. **b**, Cryo-EM micrograph of TIR-SAVED in presence of cA_3 (left panel), TIR-SAVED/cA_3 filament density map (right panel). **c**, Cryo-EM density of the final processed tetramer in two orientations. **d**, Final atomic model of TIR-SAVED with cA_3 (spacefill) located between each of the four subunits (PDB: 7QQK). **e**, Analysis of TIR-SAVED/cA_3/TIR-SAVED interaction interfaces based on the cryo-EM model. Key features and residues are highlighted. **f,** TIR domain dimer interface with NADP+ modelled inside based on structural alignment with *Vitis rotundifolia* RUN1 TIR domain (PDB: 6o0W [11]). **g**, NADase activity of D45AL46A and Y115A variants compared to WT (1.5 µM TIR-SAVED incubated with 500 µM εNAD^+ in presence of 27 µM cA_3). The mean of triplicate experiments are shown with standard deviation for the WT and Y115A variant; the inactive D45AL46A was assayed in duplicate.

Fig. 3. **TIR-SAVED oligomerisation is required for NADase activity. a**, Schematic of the assembly of TIR-SAVED variants based on *in vitro* characterisation. **b**, Electrophoretic mobility shift assay (EMSA) with radiolabelled cA_3 (alone, lane 1) incubated with TIR-SAVED wt and variants (at 0.22, 0.67, 2.0 µM). Protein/cA_3 complexes (monomers, dimers and filaments) were separated by native acrylamide gel and visualised by phosphor imaging. For gel source data, see Supplementary Fig. 1. **c**, TIR NADase activity of 0.25 µM R388E in presence of increased E84Q concentration (0, 0.125, 0.25, 0.5, 1.0, 2.0, 4.0, 8.0 µM) incubated with 500 µM εNAD^+ and 16.5 µM cA_3. As positive control, 0.25 µM WT was incubated with 8.0 µM E84Q (green bar, lane WT+E) in the same conditions. The lane R+KW corresponds to 0.25 µM R388E incubated with 2.0 µM K199E/W394A. Four experiments with standard deviation shown. **d**, Colony forming units (cfu) per milliliter of culture after plasmid immunity assay with different combinations of TIR-SAVED variants. Consistent with the *in vitro* activities, the R+E

filament was functionally active while the R+KW dimer provided no immunity. Data are means for four biological replicates. *ns* indicates *P*-values > 0.05 and * indicates *P*-values < 0.05 (based on one-way ANOVA test for multiple comparison to the R variant condition).

Fig. 4. **Multimerisation of TIR-SAVED generates a conserved composite TIR active site.** **a**, TIR-SAVED assembly generated by cA_3 promotes TIR self-association at the BE interface, composed by the BB-loop (yellow) and the DE loop. This asymmetric arrangement mediated by the BE interface is conserved in other eukaryotic TIR-enzyme assemblies like **b,** the human SARM1 complex [28] and **c,** the plant NLR RPP1 receptor [29], which are shown in the same orientation. The two-stranded TIR structure formed in the eukaryotic complexes involves the AE interface mediated by the A and E alpha helices. In TIR-SAVED filament, these two helices are oriented toward the SAVED domain.

Methods

Cloning & mutagenesis

The synthetic genes encoding *Microbacterium ketosireducens* (Mke) *cdn* and *tir-saved* were codon optimised for expression in *Escherichia coli* and purchased from Integrated DNA Technologies (IDT), Coralville, USA. Genes were cloned into the pEhisV5Tev vector [33] between the NcoI and BamHI restriction sites. The constructs were transformed into competent DH5α (*E. coli*) cells and plasmids were extracted using GeneJET plasmid miniprep kit (Thermo Scientific) to verify sequence integrity by sequencing (Eurofins Genomics). Then plasmids were transformed into *E. coli* C43 (DE3) cells for protein expression. TIR-SAVED variants, E84Q, R388E, K199E/W394A, D45AL46A and Y115A were generated on both constructs containing the *tir-saved* gene: (i) the expression vector (pEhisV5spacerTev) and (ii) the vector used for plasmid immunity assay (pRAT-Duet).

Protein expression and purification

Recombinant CD-NTase and TIR-SAVED wild-type and variants were overexpressed in *E. coli* C43 (DE3) cells. After growing at 37 °C in LB medium until OD_{600} reached 0.6-0.8, cultures were induced with 0.4 µM final IPTG concentration and incubated at 16 °C overnight. Cells were collected by centrifugation and pellets stored at -80 °C. Cell pellets were lysed by sonication in Buffer A (50 mM Tris-HCl, pH 7.5, 0.5 M NaCl, 10 mM imidazole, 10 % glycerol) supplemented by 1 $mg.mL^{-1}$ final lysozyme concentration and protease inhibitors (cOmplete, EDTA-free protease inhibitor cocktail, Roche). Clarified lysates were loaded onto a 5 mL HiTrap FF column (GE Healthcare), pre-loaded with Ni^{2+} and equilibrated with Buffer B (50 mM Tris-HCl, pH 7.5, 0.5 M NaCl, 30 mM imidazole, 10 % glycerol). Then histidine-tagged proteins were eluted along a linear gradient (50 mM to 500 mM imidazole). Recombinant histidine-tagged TEV protease was incubated with the eluted proteins to cleave the histidine-tag and the reaction was dialysed overnight at room temperature against Buffer B. Dialysed samples were loaded again onto the Ni^{2+}/loaded 5 mL HiTrap FF column (GE Healthcare) equilibrated with Buffer B. The histidine-tagged cleaved proteins passed straight through the column and were then loaded onto a 26/60 Superdex 200 size-exclusion column (GE Healthcare) equilibrated with buffer C: 20 mM Tris-HCl, pH 7.5, 0.25 M NaCl, 10% glycerol. Proteins were concentrated with 30-kDa-cutoff Amicon centrifuge filters (Millipore), flash-frozen in liquid nitrogen and stored at -80 °C. Purified protein were analysed by SDS-PAGE (NuPage Bis-Tris 4-12 %, Invitrogen) with Instant Blue staining (Expedeon Ltd). The final protein concentrations were determined by measuring absorbance at 280 nm using sequence-predicted extinction coefficients.

Cyclic nucleotide analysis by thin layer chromatography (TLC)

Synthesis of cyclic nucleotides by the CD-NTase was analysed by using α-^{32}P labelled ATP mixed with "cold" NTPs. The reactions were carried out at 37 °C for 2 h in cyclase buffer (50 mM CAPS, pH 9.4, 50 mM KCl, 10 mM $MgCl_2$, 1 mM $MnCl_2$, 1 mM DTT), as a high pH activates CD-NTases *in vitro* [34]. 20 µM CD-NTase was incubated with 50 µM ATP and 30 nM α-^{32}P-ATP in a final volume of 20 µL. Reactions were stopped by addition of phenol:chloroform and products were isolated by chloroform extraction. Then 1 µL of the final volume was spotted on a silica gel TLC plate (Supelco Sigma-Aldrich). The plate was placed into a pre-warmed humidified chamber with running buffer composed of 30 % H_2O, 70 % EtOH and 0.2 M ammonium bicarbonate, pH 9.2. Separated products were visualised by phosphor imaging. A control with a characterized Type III CRISPR system, VmeCMR [32] was performed with 1 µM purified VmeCMR, 2 µM target RNA incubated for 2 h at 37 °C in the reaction buffer (10 mM $MgCl_2$, 10 mM Tris-HCl, pH 8, 50 mM NaCl).

Cyclic nucleotide analysis by Liquid Chromatography (LC)

To analyse the nature of the cyclic nucleotide produced by the Mke CD-NTase, the reaction was carried out with 50 µM protein in cyclase buffer with 250 µM ATP for 2 h at 37 °C. The reaction was diluted 2-fold with water and ultracentrifuged using 3 kDa MWCO spin filters (Pall). Liquid chromatography analysis was performed on the Dionex UltiMate 3000 system. Sample separation occurred on a Kinetiex EVO C18 2.6 µM (2.1 x 50 mm column, Phenomenex) with a 0-8 % gradient of acetronitrile with 100 mM ammonium bicarbonate as the solvent. Flow rate was set at 300 µL min^{-1} and column compartment temperature was set at 40 °C. Data was collected at a wavelength of 250 nm and a 20 µM cA_3 commercial standard was used for comparison (Biolog).

NADase assay

The Mke TIR-SAVED NADase activity was analysed by using ε-NAD^+ as substrate – when cleaved the ε-ADP_{ribose} product could be detected by fluorescence. Reactions were prepared in a 30 µL final volume with reaction buffer (50 mM Tris-HCl, pH 7.5, 50 mM KCl, 2.5 mM $MgCl_2$), 1 µM cyclic trinucleotide (cA_3) (Biolog), 0.5 µM TIR-SAVED and 0.5 mM ε-NAD^+ (Sigma), or as stated in the figure. A master mix was prepared on ice containing protein and activator, and the substrate was added immediately before beginning analysis. Reaction samples were loaded into 96-well plates (Greiner 96 half area) and fluorescence measured continuously (cycle of 20s) over 90 min using the FluoStar Omega (BMG Labtech) with an excitation filter at 300 nm and an emission filter at 410 nm. Reactions were carried out at 28 °C. A calibration curve was evaluated with value obtained after 90 min of reaction with 10, 25, 75, 225, 500 and 675 µM ε-NAD^+ as initial concentration.

Cyclase-NADase combined assays

For the cyclase-NADase combined reaction, 5 µM CD-NTase was incubated at 37 °C with 250 µM ATP in 25 µL final volume containing 50 mM CAPS, pH 9.4, 50 mM KCl, 10 mM $MgCl_2$, 1 mM $MnCl_2$, 1 mM DTT. After 2 h, reactions were transferred into 96-well plates (Greiner 96 half area) and complemented with 0.5 µM ε-NAD^+. Fluorescence measurements were performed as mentioned above, during 10 min before adding 0.5 µM TIR-SAVED. Reactions were carried out at 37 °C for one more hour. Fluorescence data were plotted over time and analyzed with GraphPad Prism.

Plasmid immunity assays

To analyze the effect of TIR-SAVED NADase *in vivo*, we used the *Mycobacterium tuberculosis* (Mtb) Type III CRISPR system previously characterized [20] as an inducible producer of cA_3 when activated by the target RNA. Here we used the following plasmids to encode MtbCsm1-5, Cas6 and a CRISPR array: (i) pCsm1-5_ΔCsm6 (*M. tuberculosis* csm1-5 under T7 and lac promoter control) and (ii) pCRISPR_TetR (CRISPR array with tetracycline resistance gene targeting spacers and *M. tuberculosis* cas6 under T7 promoter control). Competent *E. coli* C43 (DE3) cells were co-transformed with these two constructs: pCsm1-5_ΔCsm6 and pCRISPR_TetR. Plasmids were maintained by selection with 100 $µg.mL^{-1}$ ampicillin and 50 $µg.mL^{-1}$ spectinomycin. The *tir-saved* gene was inserted into pRAT-Duet between NcoI/SalI (Multiple cloning site 1) or KpnI/BglII (Multiple cloning site 2). This plasmid contains the Tetracycline resistant gene targeted by MtbCsm. The plasmid immunity assay is based on the transformation of the target plasmid containing gene encoding TIR-SAVED into recipient cells encoding MtbCsm. How recipient cells were prepared and transformed with the target plasmid was described previously [20]. After the growth period in LB, cells were collected and resuspended in a LB volume adjusted to the same OD_{600} (about 0.1). A total of 3 µL of a 10-fold serial dilution were applied in duplicate to selective LB agar plates supplemented with 100 $µg.mL^{-1}$ ampicillin, 50 $µg.mL^{-1}$ spectinomycin, 25 $µg.ml^{-1}$ tetracycline, 0.2 % (*w/v*) D-lactose and 0.2 % *(w/v)* L-arabinose. Plates were incubated overnight at 37 °C. This experiment was performed with two independent biological replicates using two technical replicates for each experiment. The variant Cas10 D630A from MtbCsm, which abolishes cyclase activity, was used as a control for no production of cyclic-tri-AMP. For colony counting, the similar procedure was followed, except that 100 µL of a 300 µL growth volume was spread onto the selective LB agar plates. Two dilution factors were assayed for each condition and the experiments were performed in biological triplicates. Following incubation at 37 °C for 17-18 h, the resulting colonies were manually counted and the number of colony forming unit (cfu) reported per milliliter of culture volume. Data were statistically analysed by Prism8 (GraphPad) using a non-

pairing Brown-Forsythe and Welch ANOVA tests. For multiple comparisons, the Dunnett T3 test was used.

Analytical gel filtration

To analyze the oligomeric state of TIR-SAVED, 100 µL protein (at least 100 µM) was injected into a size exclusion column (Superose 6 Increase 10/300 GL or Superose 12, GE Healthcare) equilibrated in 20 mM Tris-HCl, pH 8.0, 250 mM NaCl and 10 % glycerol. When indicated in the figure, 158 µM cyclic-tri-AMP (cA_3) was added to the TIR-SAVED sample before centrifugation at 10,000 *x g* for 10 min at 4 °C and loaded onto the size exclusion column. To analyse TIR-SAVED dimerization, 83 µM R388E variant was firstly incubated with 500 µM cA_3 and 127 µM K199E/W394A variant and loaded into the Superose 12 size exclusion column in similar conditions. The eluted fractions were then analysed by native PAGE in a 4-16 % Bis-Tris gel (Invitrogen).

Using similar gel filtration running conditions, standard proteins (#1511901, BioRad) were eluted to calculate a calibration curve of the column. 100 µL BSA (7.3 $mg.mL^{-1}$) was injected as an additional standard. The elution volume (V_e) for each protein was determined based on the elution profile. Then the $K_{average}$ (K_{av}) was calculated as the ratio: $K_{average} = (V_e-V_0)/(V_t-V_0)$ where V_0 is the void volume (7.77 mL) and V_t the total volume (24 mL) of the column. The calibration curve corresponds to the K_{av} plot *versus* the molecular weight of each protein in Log_{10}. The trendline (logarithmic) was plotted with the following standard: y-globulin (158 kDa), BSA (66 kDa), ovalbumin (44 kDa) and myoglobin (17 kDa) to get the best R^2 value (0.997) corresponding to the range of the target protein.

Dynamic light scattering (DLS)

DLS measurements were performed with the Zetasizer Nano S90 (Malvern) instrument. In the protein dilution buffer (20 mM Tris-HCl, pH 7.5, 250 mM NaCl, 10 % glycerol), 21 µM TIR-SAVED was prepared with 32 µM cyclic nucleotide (cyclic-tri-AMP or others) when stated in the figure. After centrifugation at 12,000 xg for 10 min at 4 °C and filtration with 0.22 µm filters, 12 µL of sample was loaded into the quartz cuvette (ZMV1012). The measurements were done at 25 °C with three measures of thirteen runs. The curves of TIR-SAVED WT are the mean of 3 technical replicates and 2 independent experiments.

Small-angle X-ray scattering

SAXS datasets were recorded at the European Synchrotron Radiation Facility (ESRF, Grenoble, France) on the BioSAXS beamline BM29 [35] using a 2D Pilatus detector. Data were collected at room temperature (20 °C) using a standard set up (automated sample mounting to a capillary by a robot)[36]. 100 µL TIR-SAVED (10.9 $mg.mL^{-1}$) was injected into the Superose

12 column 10/300 GL (GE Healthcare) in 20 mM Tris-HCl, pH 8.0, 250 mM NaCl and 10 % glycerol with a flow rate of 0.4 mL/min.

Sample scattering curves were obtained after subtraction of the averaged buffer signals using standard protocols with PRIMUS [37]. The Rg and I(0) values were extracted using the Guinier approximation. The molecular weight range was estimated by Bayesian inference[38] implemented in the ATSAS suite 3.0.5 [39]. Theoretical SAXS curve of the TIR-SAVED AF2 predicted structure was back-calculated and fitted with the experimental SAXS datasets with the program CRYSOL [40]. SAXS parameters for data collection and analysis are reported in Supplementary Data, Table 1.

Electrophoretic mobility shift assays

Radiolabelled α-^{32}P-cA_3 was prepared with the Type III CRISPR complex, VmeCMR, as described in the "Cyclic nucleotide analysis by thin layer chromatography (TLC)" section. The reaction product was incubated with a 3-fold dilution range of TIR-SAVED (0.22, 0.67, 2.0 µM) for 15 min at 25 °C in a final 15 µL volume. The reaction buffer was the same as for NADase activity: 50 mM Tris-HCl, pH 7.5, 50 mM KCl, 2.5 mM $MgCl_2$ and 25 mM NaCl from the protein dilution buffer. Ficoll was added to the samples to get 4 % as final concentration and samples were then loaded into a native 6 % acrylamide gel (acrylamide:bis-acrylamide 29:1). TIR-SAVED/cA_3 complexes were separated by electrophoresis into 1X TBE buffer for 1 h at 200 V and visualized by phosphor imaging.

Thermal shift assays

2 µM TIR-SAVED WT or variants were incubated with a range of cA_3 concentration (0, 0.4, 2, 10 µM) in the following buffer: 20 mM Tris-HCl, pH 7.5, 250 mM NaCl, 10 % glycerol supplemented by and 5X SYPRO Orange Fluorescent Dye (BioRad). A temperature gradient was applied from 25 to 95 °C with 1 °C increments and fluorescence measured in a Stratagene MX3005. The curves are the mean of two independent experiments with technical triplicates.

Transmission electron microscopy

Samples for screening negative-stain electron microscopy analysis were prepared by diluting purified TIR-SAVED protein alone, or with an equimolar ratio of cyclic trinucleotide as indicated, to a concentration of 1 mg/ml in buffer (20 mM Tris-HCl pH 8.0, 250 mM NaCl, 10 % glycerol). Electron microscopy images of negatively stained TIR-SAVED were collected using an JEOL 1200 transmission electron microscope operating at 120 keV and equipped with a Gatan Orius CCD camera at a nominal magnification of 100K ×, pixel size of 9.6 Å. 4 µl of the diluted sample was applied onto a glow-discharged 400-mesh copper grid (agar Scientific) coated with a layer of continuous carbon, followed by a 1 min absorption step and side blotting to remove bulk

solution. The grid was immediately stained with 2 % uranyl acetate at pH 7 and then blotted from the side and air dried prior to imaging.

Cryo-electron microscopy grids were prepared using a FEI Vitrobot Mark IV (Thermo Fisher Scientific Ltd) at 4 °C and 95 % humidity. 3 µl of TIR-SAVED complex was applied to Holey Carbon grids (Quantifoil Cu R1.2/1.3, 300 mesh), glow discharged for 45 s at current of 45 mA in a EMITECH K100X glow discharger. The grids were then blotted with filter paper once to remove any excess sample, and plunge-frozen in liquid ethane. All cryo-EM data presented here were collected on JEOL CRYO ARM 300 microscope, equipped with a DE-64 direct detector at the Scottish Centre for Macromolecular Imaging, Glasgow, UK. 3,907 movies were collected in accurate hole centering mode using SerialEM 3.8 [41]. The CryoSPARC 3.3.1 software [42] was used for motion correction, CTF estimation and manual exposure correction, as well as for the choice of the 2,319 movies used in the analysis. CryoSPARC 3.3.1 was also used for the whole single particle reconstruction workflow, from manual particle picking to classification to generate templates for autopicking and subsequent 2D classification and 3D processing, including per-particle motion correction [43], sharpening and 3D variability analysis [44] obtaining a structure with overall resolution of 3.8 Å. The final reconstruction was obtained from 596,378 particles selected from classes representing both circular and elongated particles at a 0.997 Å/pixel sampling and had overall resolution of 3.8 Å, as calculated by Fourier shell correlation at 0.143 cut-off during post-processing. The AF2 model was fitted to the map using the Chimera software, taking into account both hands. The inverted hand was the only compatible solution and was therefore chosen for further modelling and refinement using the Coot [45], Refmac-Servalcat as implemented in the CCP-EM suite [46] and PHENIX [47] software packages. The cryo-EM data collection, refinement and validation statistics are summarised in Extended Data Fig. 10.

References

35 Pernot, P. *et al.* Upgraded ESRF BM29 beamline for SAXS on macromolecules in solution. *J Synchrotron Radiat* **20**, 660-664, doi:10.1107/S0909049513010431 (2013).

36 Round, A. *et al.* BioSAXS Sample Changer: a robotic sample changer for rapid and reliable high-throughput X-ray solution scattering experiments. *Acta Crystallographica Section D-Structural Biology* **71**, 67-75, doi:10.1107/S1399004714026959 (2015).

37 Costa, L. *et al.* Combined small angle X-ray solution scattering with atomic force microscopy for characterizing radiation damage on biological macromolecules. *BMC Struct Biol* **16**, 18, doi:10.1186/s12900-016-0068-2 (2016).

38 Hajizadeh, N. R., Franke, D., Jeffries, C. M. & Svergun, D. I. Consensus Bayesian assessment of protein molecular mass from solution X-ray scattering data. *Scientific reports* **8**, 7204, doi:10.1038/s41598-018-25355-2 (2018).

39 Manalastas-Cantos, K. *et al.* ATSAS 3.0: expanded functionality and new tools for small-angle scattering data analysis. *Journal of Applied Crystallography* **54**, 343-355, doi:10.1107/S1600576720013412 (2021).

40 Svergun, D., Barberato, C. & Koch, M. H. J. CRYSOL - A program to evaluate x-ray solution scattering of biological macromolecules from atomic coordinates. *Journal of Applied Crystallography* **28**, 768-773, doi:Doi 10.1107/S0021889895007047 (1995).
41 Mastronarde, D. N. Automated electron microscope tomography using robust prediction of specimen movements. *Journal of structural biology* **152**, 36-51, doi:10.1016/j.jsb.2005.07.007 (2005).
42 Punjani, A., Rubinstein, J. L., Fleet, D. J. & Brubaker, M. A. cryoSPARC: algorithms for rapid unsupervised cryo-EM structure determination. *Nat Methods* **14**, 290-296, doi:10.1038/nmeth.4169 (2017).
43 Rubinstein, J. L. & Brubaker, M. A. Alignment of cryo-EM movies of individual particles by optimization of image translations. *Journal of structural biology* **192**, 188-195, doi:10.1016/j.jsb.2015.08.007 (2015).
44 Punjani, A. & Fleet, D. J. 3D variability analysis: Resolving continuous flexibility and discrete heterogeneity from single particle cryo-EM. *Journal of structural biology* **213**, 107702, doi:10.1016/j.jsb.2021.107702 (2021).
45 Casanal, A., Lohkamp, B. & Emsley, P. Current developments in Coot for macromolecular model building of Electron Cryo-microscopy and Crystallographic Data. *Protein Sci* **29**, 1069-1078, doi:10.1002/pro.3791 (2020).
46 Nicholls, R. A., Tykac, M., Kovalevskiy, O. & Murshudov, G. N. Current approaches for the fitting and refinement of atomic models into cryo-EM maps using CCP-EM. *Acta Crystallogr D Struct Biol* **74**, 492-505, doi:10.1107/S2059798318007313 (2018).
47 Liebschner, D. *et al.* Macromolecular structure determination using X-rays, neutrons and electrons: recent developments in Phenix. *Acta Crystallogr D Struct Biol* **75**, 861-877, doi:10.1107/S2059798319011471 (2019).

Acknowledgements

This work was funded by the BBSRC (ref. BB/S000313 and BB/T004789) and a European Research Council Advanced Grant (grant number 101018608) to MFW. We thank Dr Januka Athukoralage, Dr Tracey Gloster and Mr Stuart McQuarrie for discussions. We thank M. Tully for assistance in using beamline BM29. We acknowledge the Scottish Centre for Macromolecular Imaging (SCMI), Dr Mairi Clarke and Dr James Streetley for assistance with cryo-EM experiments and access to instrumentation, funded by the MRC (MC_PC_17135) and SFC (H17007). This work used the platforms of the Grenoble Instruct-ERIC center (ISBG; UAR 3518 CNRS-CEA-UGA-EMBL) within the Grenoble Partnership for Structural Biology (PSB), supported by FRISBI (ANR-10-INBS-0005-02) and GRAL, financed within the University Grenoble Alpes graduate school (Ecoles Universitaires de Recherche) CBH-EUR-GS (ANR-17-EURE-0003).

Author Contributions

G.H. planned, carried out and analysed the biochemical experiments and structural analyses and drafted the manuscript; A.G. collected and analysed Electron Microscopy data; S. G. cloned, expressed and purified the wild-type and variant proteins; H.R. carried out the preliminary biochemical analysis of the effector protein; S.Gu analysed the cyclic nucleotides; Q.B. carried out the SAXS; L.S. planned and analysed the EM analyses; M.F.W.

conceptualised and oversaw the project, obtained funding and analysed data along with the other authors. All authors contributed to the drafting and revision of the manuscript.

Additional information

Supplementary information is available for this paper.

Correspondence and requests for materials should be addressed to Malcolm White (mfw2@st-andrews.ac.uk).

Competing interest statement

The authors declare they have no competing interests.

Data Availability

The electron microscopy data deposition D_1292120121 is assigned the following accession code(s): PDB ID 7QQK, EMD-14122. All other data are provided in Supplementary Information.

Extended Data Figure Legends

Extended data Fig. 1. Cyclase and NADase activity. a, Cyclase products separated by thin layer chromatography. Radiolabelled ATP was mixed with 50 μM "cold" NTP (ATP, GTP, CTP, TTP, or UTP) and incubated with 20 μM cyclase for 2 h at 37 °C. As controls, cyclic oligoadenylate produced by the Type III CRISPR complex VmeCMR [21] (C^+) and the reaction without protein (C^-). **b,** Cyclic nucleotide screening for TIR-SAVED NADase activity. 0.5 μM TIR-SAVED was incubated without (apo condition) or with 5 μM cyclic: AMP, di-AMP, tri-AMP, tetra-AMP, hexa-AMP, GMP, di-GMP, AMP-GMP, di-AMP-GMP or ADPribose. The fluorescence intensity (a.u.) at 90 min of reaction was plotted for each cyclic oligoadenylate. **c**, Initial rate of TIR NADase activity depends on cA_3 concentration. 0.5 μM TIR-SAVED was incubated with 0, 0.1, 0.3, 0.5, 1.0, 2.5 μM cA_3 and 500 μM εNAD^+. **d**, Enzymatic characterization of TIR-SAVED NADase activity. Initial rate is plotted against a range of εNAD^+ concentration. Experimental data were fitted using the Michaelis-Menten equation. **e**, TIR NADase activity is proportional to TIR-SAVED concentration. 0, 0.1, 0.2, 0.4, 0.5, 0.8, 1.0 μM TIR-SAVED were incubated with 1 μM cA_3 and 2 mM εNAD^+. Data are the means of triplicate experiments with standard deviation (b, c, d, e).

Extended Data Fig. 2. Plasmid immunity assay with TIR-SAVED activated by Type III CRISPR CSM. Extended dataset from Fig. 1.g. **a**, Schematic of the plasmid and competent cells used for the transformation. On the left, tetracycline resistant plasmid used for to transform the recipient cell. The tir-saved gene was cloned into the multiple cloning site 1 of the plasmid 2 and 3. In the plasmid 3, the catalytic residue E84 was mutated to prevent

NADase activity. Recipient cell A and B both expressed the MtbCsm targeting the tetracycline resistant plasmid. In B, MtbCsm Cas10 was mutated (D630A) to prevent cOA production and is used as a control. In recipient cell C, the tetracycline resistant plasmid is not recognized as a target by MtbCsm. **b**, Cloning strategy of TIR-SAVED variants into the pRAT-Duet plasmid (left panel). To co-express two TIR-SAVED variants, one version was cloned into the multiple cloning site 1 (MSC-1) under the pBAD promotor while the R variant was cloned into the multiple cloning site 2 (MSC-2) under the T7 promoter. **c**, Transformed colonies after incubation overnight on induced plate. The different recipient cell/plasmid combination are annotated as "A.1" (recipient cell A transformed by plasmid 1). Results from two independent experiments with technical duplicates.

Extended Data Fig. 3. TIR-SAVED is a monomeric protein in diluted solution. a, SEC-SAXS profile. Rg (radiation gyrus) was calculated based on Guinier approximation (see Material & Method section) and plotted against eluted volume. In red, the fractions used to estimate the global Rg and the molecular weight range of the protein. The theoretical MW value of the recombinant TIR-SAVED is 47.3 kDa. **b**, AF2 model fitted with the SEC-SAXS experimental dataset selected (red fractions in a.). **c**, Elution profile of TIR-SAVED after size exclusion chromatography in absence (blue) or presence (orange) of cA_3 for a molar ratio of 1:1.5 (protein:cA_3). Additional analysis of TIR-SAVED molecular weight by analytical gel filtration are shown in Supplemental Data Fig. 4.

Extended Data Fig. 4. Cryo-EM analysis of the TIR-SAVED filament. a, Cryo-EM micrograph with single particle picked. **b,** Extract of single particle selected. **c,** 2D classes from both top and side views particles. **d,** 3D model of the filament. In blue, the extracted map used for refinement. **e,** Final refined 3D map coloured by local resolution (blue 2.5 A to red, 5 Å). **f**, Atomic model fitted into the density map for four TIR-SAVED/cA_3 subunits.

Extended Data Fig.5. Surface representation of one TIR-SAVED subunit. a, position of the cA_3 molecule bound to the SAVED protein. **b**, Representative map densities. Example map densities that allowed construction of the atomic model. The labels refer to the chain identities and residue numbers. The regions part of TIR-SAVED main features (BB loop, DE loop and cA_3 binding pocket) are highlighted.

Extended Data Fig.6. Sequence alignment of TIR-SAVED proteins. Secondary structure features are displayed for the TIR domain to match the conserved features of protein TIR family. Conserved residues are shaded. Mutated residues used in biochemical experiments are highlighted.

Extended Data Fig.7. Activity and oligomerisation of TIR mutants. a, Dynamic Light Scattering analysis confirms the oligomerisation of Y115A and D45AL46A in presence of 1:1.5

protein:cA_3 molar ratio. Experiment in technical triplicates for each condition. **b**, NADase activity comparison of the Y115A and D45AL46A mutants with the WT for a 3-fold serial dilution in protein concentrations (0.16, 0.5, 1.5, 4.5, 13.5 µM). 27 µM cA_3 was used to activate TIR-SAVED incubated with 500 µM εNAD^+ substrate. **c**, Enzymatic properties of Y115A mutant. Based on a NAD range concentration experiment, the initial rate of fluorescent ADP ribose production was calculated and fitted following a Michaelis-Menten model. In these experiments, as used previously for the WT, 0.5 µM Y115A was mixed in presence of 1 µM cA_3 to hydrolyse 25, 75, 225, 500, 1000, 1500, 2000 and 3000 µM εNAD^+. The right panel compares the final Michaelis-Menten parameters of Y115A with the WT protein. Data are the means of three experiments with Standard deviation indicated.

Extended Data Fig. 8. cA_3 binding properties of TIR-SAVED mutant R388E and W394A. **a**, Schematic of TIR-SAVED mutations. **b,** Dynamic Light Scattering profile of TIR-SAVED variants in presence of 1:1.5 protein:cA_3 molar ratio. **c**, NADase activity of E84Q and R388E compared to the WT TIR-SAVED enzyme. A range of protein concentration (0, 0.16, 0.5, 1.5, 4, 13.5 µM) was incubated with 27 µM cA_3 and 500 µM ε-NAD^+ for 60 min. Data are means plotted with standard deviations for triplicate experiments. **d,** The K199E/W394A variant is catalytically dead. The protein (1.5 µM) was incubated with increased cA_3 concentration (from 0.03 to 13.5 µM) and 500 µM ε-NAD^+. Data are means from duplicate experiments. **e,** Comparison of the thermal denaturation profile of TIR-SAVED in presence of three concentrations of cA_3 indicated as protein:cA_3 molar ratio of 1:0.2, 1:1, 1:5. The melting temperature Tm for the condition 1:0 and 1:5 was plotted for each protein (right panel). Experiments were done in triplicates with three measures for each temperature.

Extended Data Fig. 9. Combination of TIR-SAVED variants. a, Purification by gel filtration of the dimeric TIR-SAVED variant in comparison to the wild-type apo protein. The R388E variant (R) was incubated with K199E/W394A (KW) in presence of cA_3. **b**, Analysis of the eluted fraction from (a) by native PAGE. As controls, separated TIR-SAVED were loaded in absence or presence of cA_3. **c**, The combination of R+KW is catalytically dead. The R variant (0.25 µM) was incubated with increased KW concentration (from 0.125 to 2 µM) in presence of 4.5 µM cA_3 and 500 µM ε-NAD^+**. d**, Kinetic analysis of subunit mixing experiments over 60 min. The WT+E and R+E combinations yielded similar activation kinetics. At later time points, weak activation was observed for the KW+E combination, whilst the E and KW controls showed no activity. In each mixing experiment, the indicated variant (0.25 µM) was incubated with 8 µM E variant in presence of 16.5 µM cA_3.

Extended Data 10. Cryo-EM data collection, refinement and validation statistics

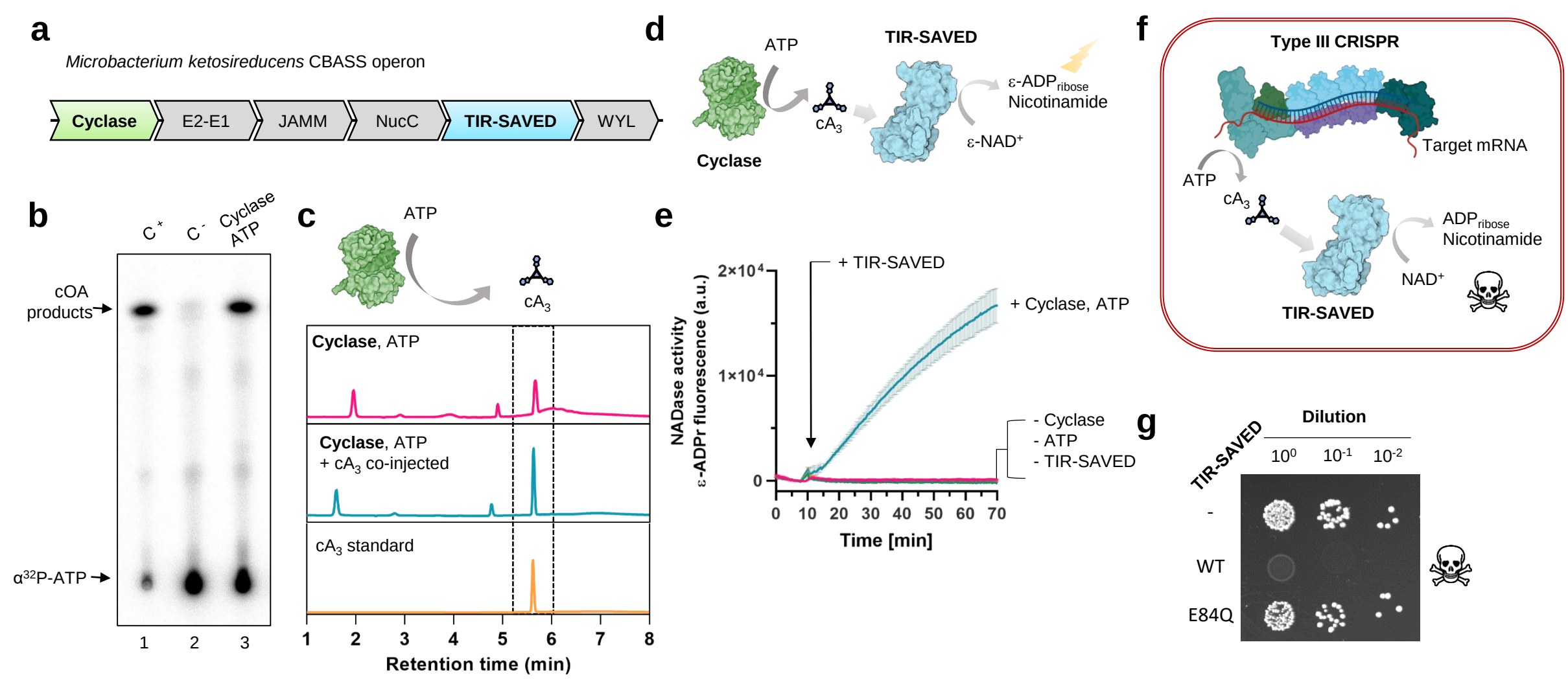
a
Microbacterium ketosireducens CBASS operon
Cyclase
E2-E1
JAMM
NucC
TIR-SAVED
WYL
b
C+
C-
Cyclase ATP
cOA products
α32P-ATP
1
2
3
c
ATP
cA3
Cyclase, ATP
Cyclase, ATP
+ cA3 co-injected
cA3 standard
1
2
3
4
5
6
7
8
Retention time (min)
d
ATP
TIR-SAVED
cA3
Cyclase
ε-ADPribose
Nicotinamide
ε-NAD+
e
+ TIR-SAVED
+ Cyclase, ATP
- Cyclase
- ATP
- TIR-SAVED
NADase activity
ε-ADPr fluorescence (a.u.)
2×10⁴
1×10⁴
0
0
10
20
30
40
50
60
70
Time [min]
f
Type III CRISPR
Target mRNA
ATP
cA3
ADPribose
Nicotinamide
NAD+
TIR-SAVED
g
Dilution
TIR-SAVED
10⁰
10⁻¹
10⁻²
-
WT
E84Q

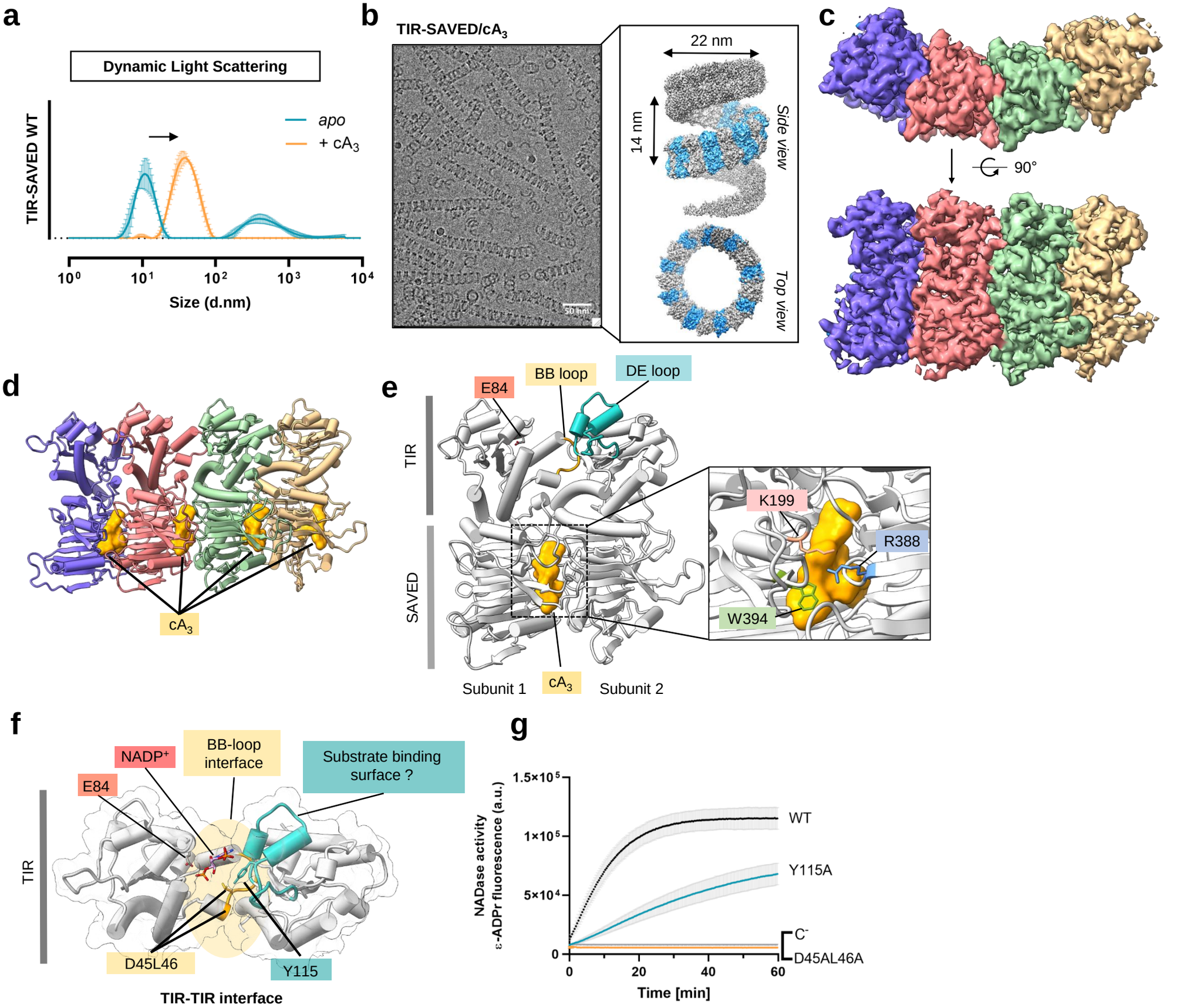
a
Dynamic Light Scattering
TIR-SAVED WT
apo
+ cA3
10^0
10^1
10^2
10^3
10^4
Size (d.nm)
b
TIR-SAVED/cA3
50 nm
22 nm
14 nm
Side view
Top view
c
90°
d
cA3
e
E84
BB loop
DE loop
TIR
SAVED
K199
R388
W394
Subunit 1
cA3
Subunit 2
f
NADP+
BB-loop interface
Substrate binding surface ?
E84
TIR
D45L46
Y115
TIR-TIR interface
g
NADase activity ε-ADPr fluorescence (a.u.)
1.5×10^5
1×10^5
5×10^4
0
WT
Y115A
C-
D45AL46A
0
20
40
60
Time [min]

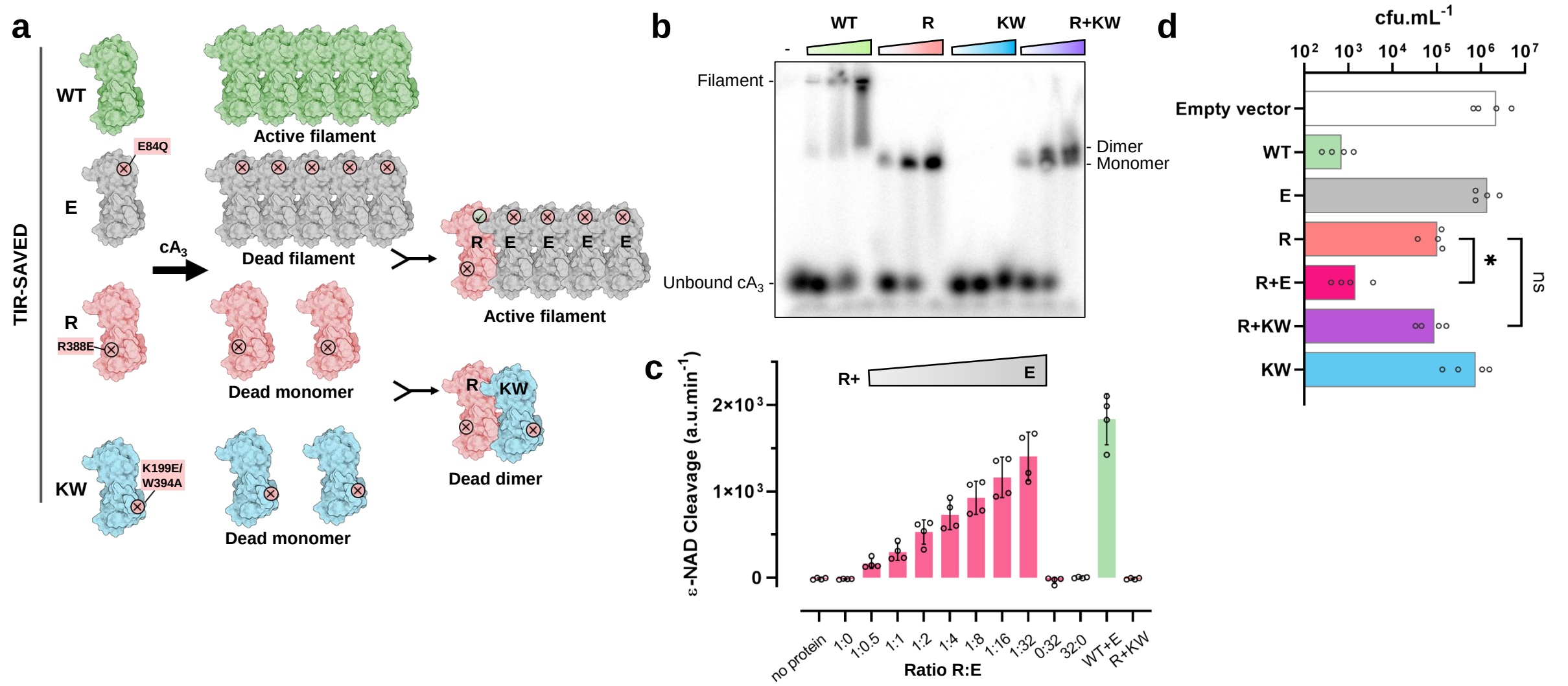
a
TIR-SAVED
WT
Active filament
E84Q
E
cA3
Dead filament
R E E E E
Active filament
R
R388E
Dead monomer
R KW
Dead dimer
K199E/
W394A
KW
Dead monomer
b
WT
R
KW
R+KW
-
Filament
Unbound cA3
Dimer
Monomer
c
R+
E
ε-NAD Cleavage (a.u.min-1)
2×10 3
1×10 3
0
no protein
1:0
1:0.5
1:1
1:2
1:4
1:8
1:16
1:32
0:32
32:0
WT+E
R+KW
Ratio R:E
d
cfu.mL-1
10 2
10 3
10 4
10 5
10 6
10 7
Empty vector
WT
E
R
R+E
R+KW
KW
*
ns

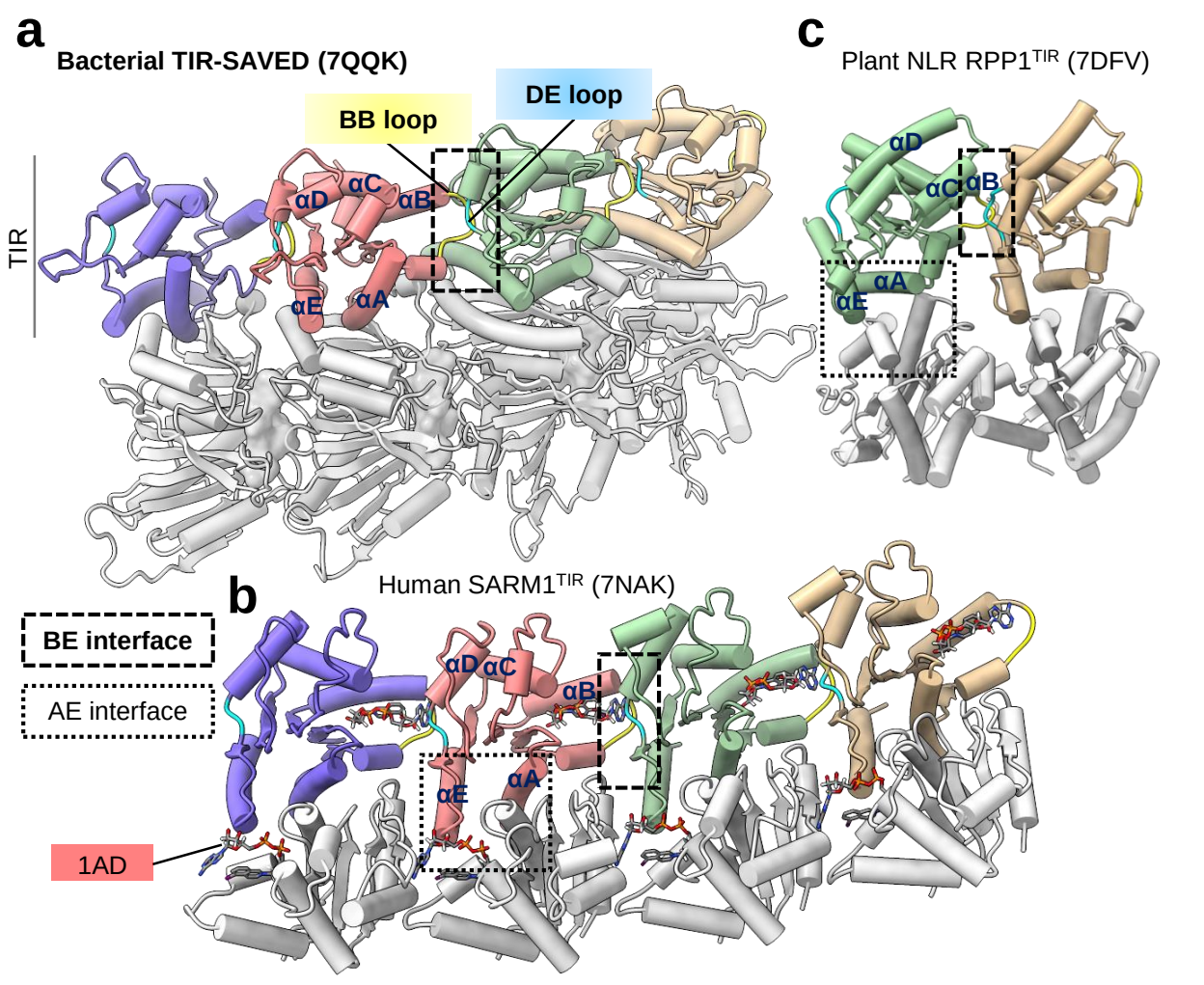
a
Bacterial TIR-SAVED (7QQK)
BB loop
DE loop
TIR
αD
αC
αB
αE
αA
c
Plant NLR RPP1TIR (7DFV)
αD
αC
αB
αA
αE
b
Human SARM1TIR (7NAK)
BE interface
AE interface
αD
αC
αB
αA
αE
1AD

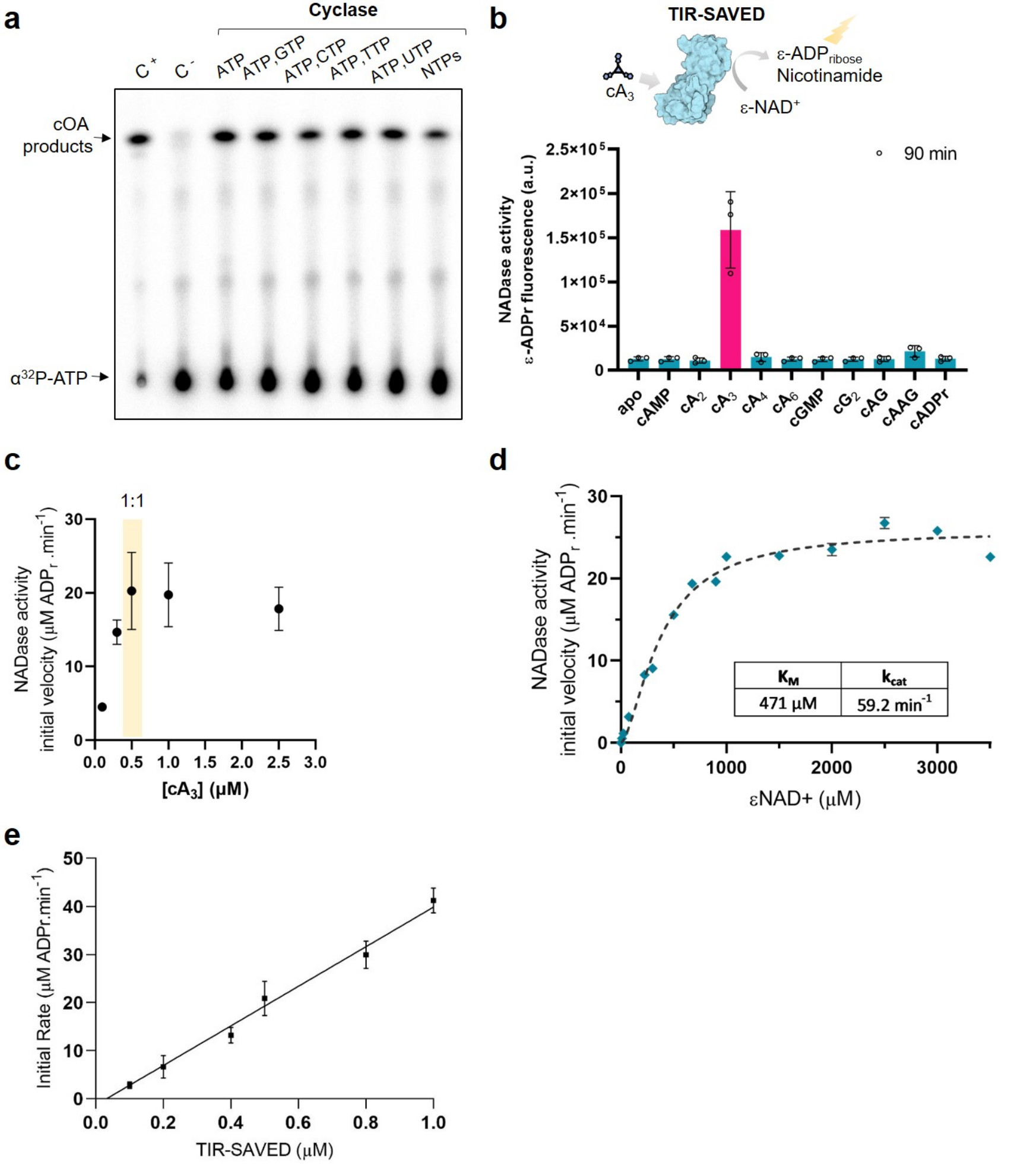
a
Cyclase
C+
C-
ATP
ATP,GTP
ATP,CTP
ATP,TTP
ATP,UTP
NTPs
cOA products
α32P-ATP
b
TIR-SAVED
cA3
ε-ADPribose
Nicotinamide
ε-NAD+
90 min
NADase activity
ε-ADPr fluorescence (a.u.)
2.5×10^5
2×10^5
1.5×10^5
1×10^5
5×10^4
0
apo
cAMP
cA2
cA3
cA4
cA6
cGMP
cG2
cAG
cAAG
cADPr
c
1:1
NADase activity
initial velocity (μM ADPr.min-1)
30
20
10
0
0.0
0.5
1.0
1.5
2.0
2.5
3.0
[cA3] (μM)
d
NADase activity
initial velocity (μM ADPr.min-1)
30
20
10
0
0
1000
2000
3000
εNAD+ (μM)
KM
kcat
471 μM
59.2 min-1
e
Initial Rate (μM ADPr.min-1)
50
40
30
20
10
0
0.0
0.2
0.4
0.6
0.8
1.0
TIR-SAVED (μM)

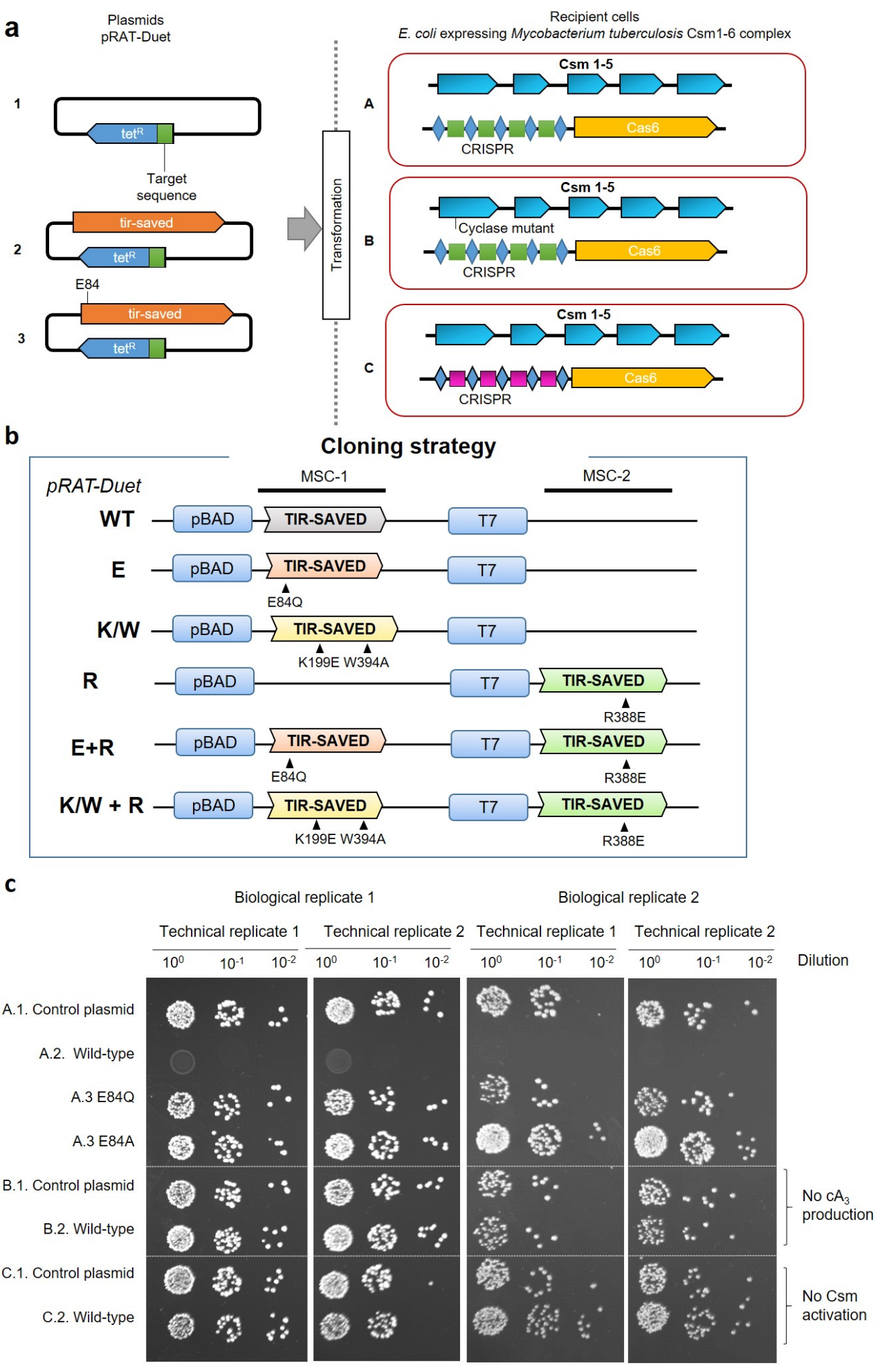
a
Plasmids
pRAT-Duet
Recipient cells
E. coli expressing Mycobacterium tuberculosis Csm1-6 complex
1
tetR
Target
sequence
2
tir-saved
tetR
E84
3
tir-saved
tetR
Transformation
A
Csm 1-5
Cas6
CRISPR
B
Csm 1-5
Cyclase mutant
Cas6
CRISPR
C
Csm 1-5
Cas6
CRISPR
b
Cloning strategy
pRAT-Duet
MSC-1
MSC-2
WT
pBAD
TIR-SAVED
T7
E
pBAD
TIR-SAVED
T7
E84Q
K/W
pBAD
TIR-SAVED
T7
K199E W394A
R
pBAD
T7
TIR-SAVED
R388E
E+R
pBAD
TIR-SAVED
T7
TIR-SAVED
E84Q
R388E
K/W + R
pBAD
TIR-SAVED
T7
TIR-SAVED
K199E W394A
R388E
c
Biological replicate 1
Biological replicate 2
Technical replicate 1
Technical replicate 2
Technical replicate 1
Technical replicate 2
10^0 10^-1 10^-2
10^0 10^-1 10^-2
10^0 10^-1 10^-2
10^0 10^-1 10^-2
Dilution
A.1. Control plasmid
A.2. Wild-type
A.3 E84Q
A.3 E84A
B.1. Control plasmid
B.2. Wild-type
C.1. Control plasmid
C.2. Wild-type
No cA3 production
No Csm activation

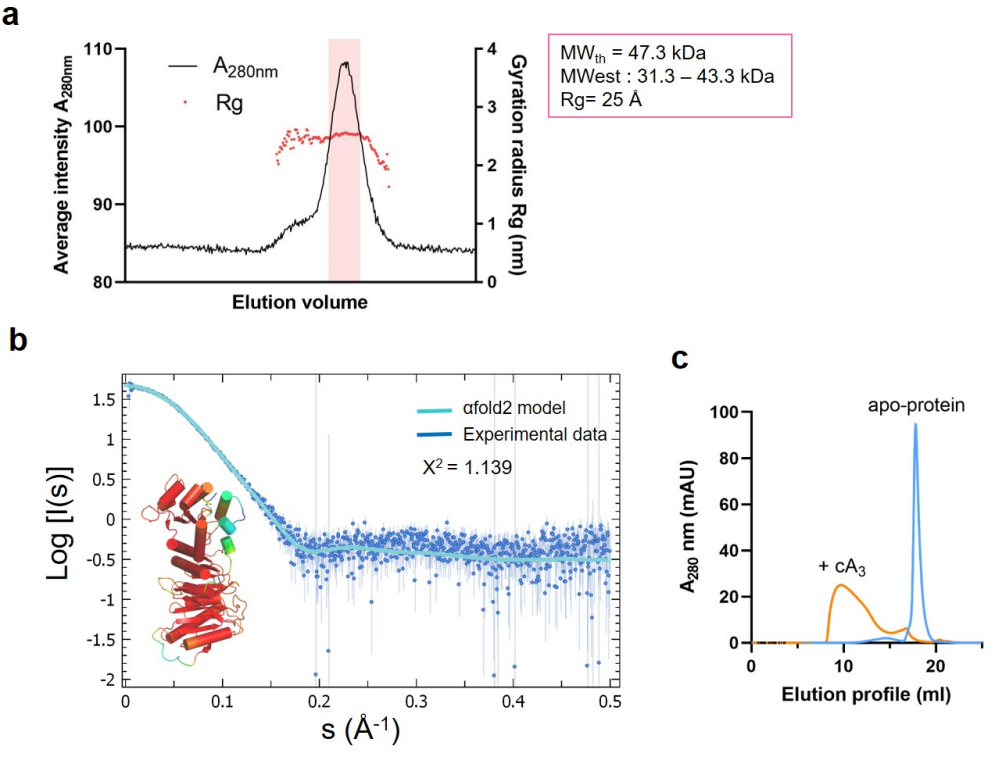
a
110
100
90
80
A280nm
Rg
Average intensity A280nm
Gyration radius Rg (nm)
4
3
2
1
0
Elution volume
MWth = 47.3 kDa
MWest : 31.3 – 43.3 kDa
Rg= 25 Å
b
Log [I(s)]
1.5
1
0.5
0
-0.5
-1
-1.5
-2
αfold2 model
Experimental data
X2 = 1.139
0
0.1
0.2
0.3
0.4
0.5
s (Å-1)
c
apo-protein
+ cA3
A280 nm (mAU)
100
80
60
40
20
0
0
10
20
Elution profile (ml)

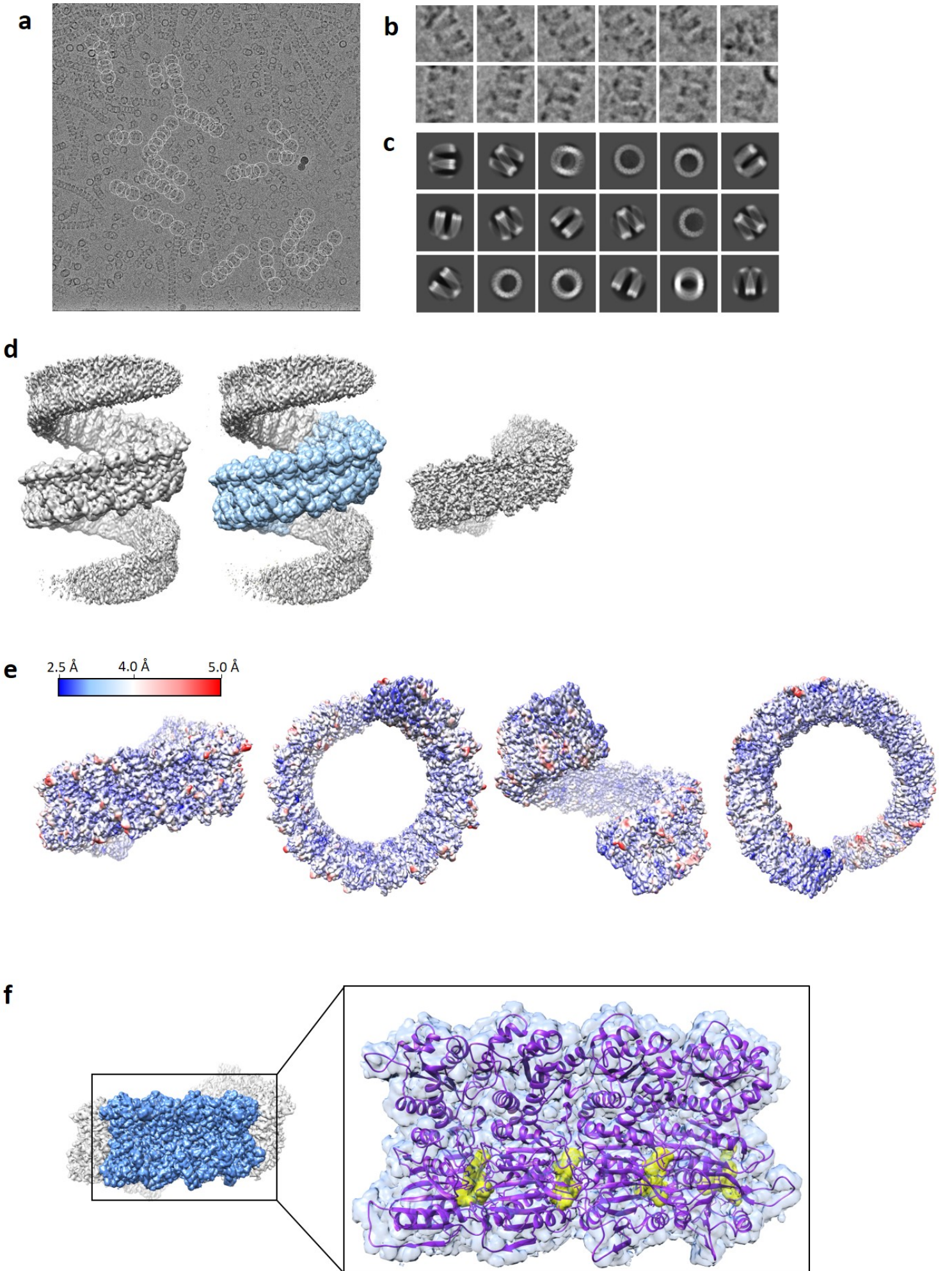
a
b
c
d
e
2.5 Å
4.0 Å
5.0 Å
f

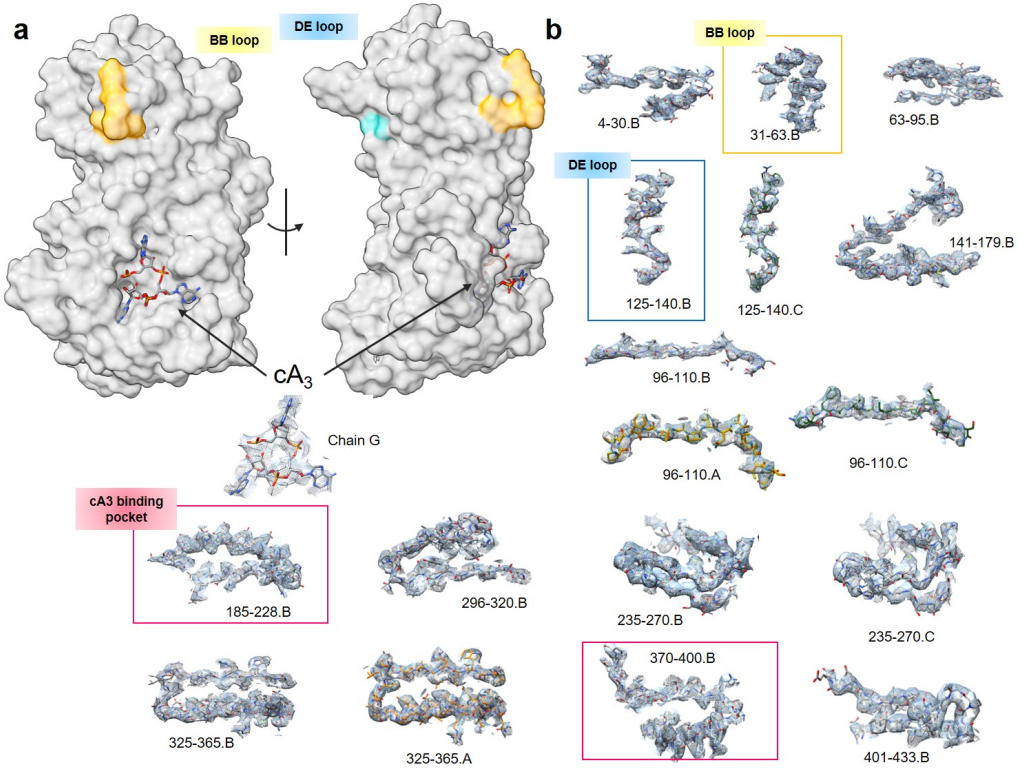
a
BB loop
DE loop
cA3
Chain G
cA3 binding pocket
185-228.B
296-320.B
325-365.B
325-365.A
b
BB loop
4-30.B
31-63.B
63-95.B
DE loop
125-140.B
125-140.C
141-179.B
96-110.B
96-110.A
96-110.C
235-270.B
235-270.C
370-400.B
401-433.B

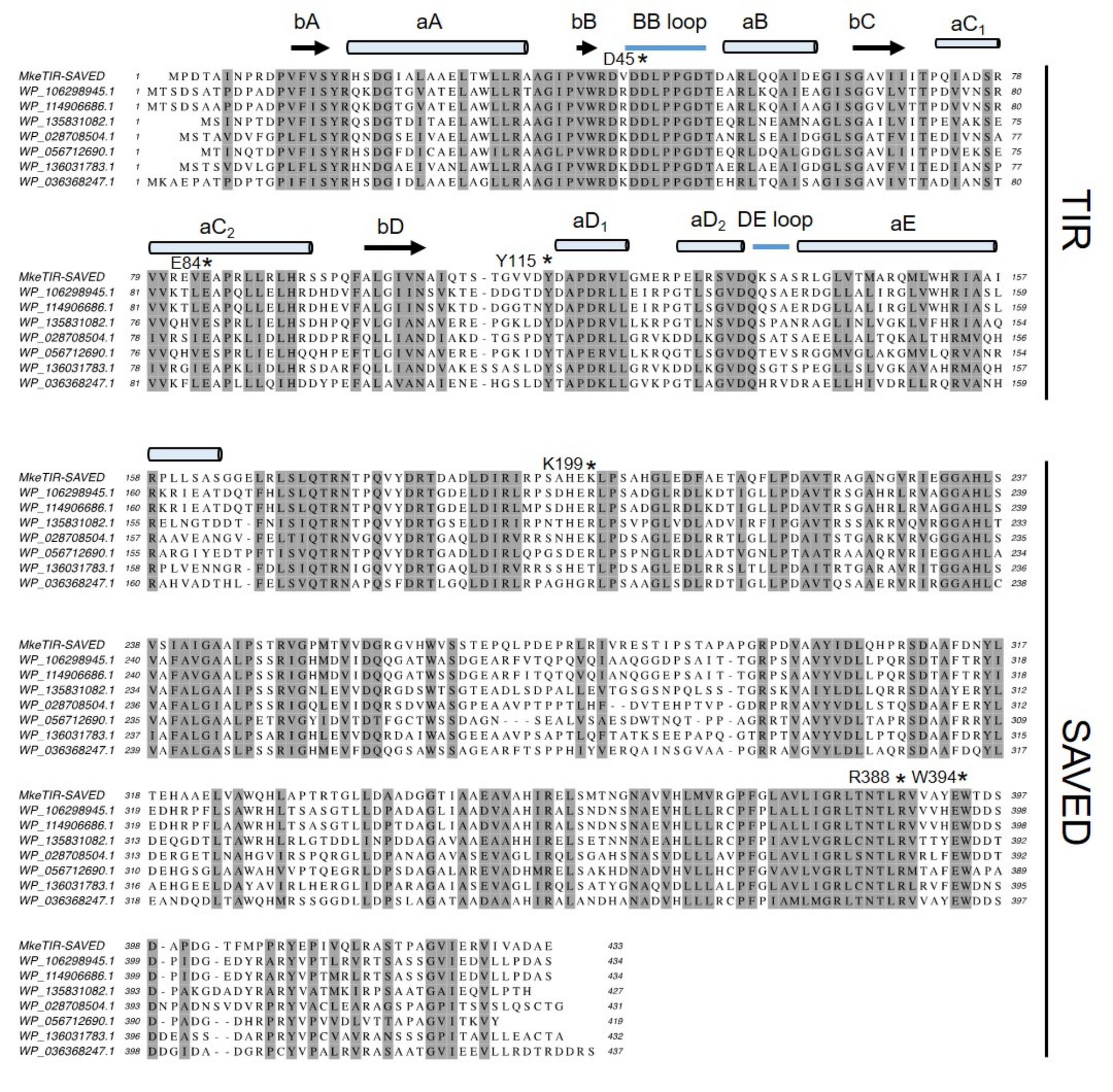
bA
aA
bB
BB loop
aB
bC
aC1
D45*
MkeTIR-SAVED 1 MPDTAINPRDPVFVSYRHSDGIALAAELTWLLRAAGIPVWRDVDDLPPGDTDARLQQAIDEGISGAVIIITPQIADSR 78
WP_106298945.1 1 MTSDSATPDPADPVFISYRQKDGTGVATELAWLLRTAGIPVWRDRDDLPPGDTEARLKQAIEAGISGGVLVTTPDVVNSR 80
WP_114906686.1 1 MTSDSAAPDPADPVFISYRQKDGTGVATELAWLLRAAGIPVWRDRDDLPPGDTEARLKQAIAAGISGGVLVTTPDVVNSR 80
WP_135831082.1 1 MSINPTDPVFISYRQSDGTDITAELAWLLRAAGIPVWRDRDDLPPGDTEQRLNEAMNAGLSGAILVITPEVAKSE 75
WP_028708504.1 1 MSTAVDVFGPLFLSYRQNDGSEIVAELAWLLRAAGIPVWRDKDDLPPGDTANRLSEAIDGGLSGATFVITEDIVNSA 77
WP_056712690.1 1 MTINQTDPVFISYRHSDGFDICAELAWILRAAGLPVWRDRDDLPPGDTEQRLDQALGDGLSGAVLIITPDVEKSE 75
WP_136031783.1 1 MSTSVDVLGPLFLSYRHNDGAEIVANLAWLLRAAGIPVWRDKDDLPPGDTAERLAEAIGDGLSGAVFVITEDIANSP 77
WP_036368247.1 1 MKAEPATPDPTGPIFISYRHSDGIDLAAELAGLLRAAGIPVWRDKDDLPPGDTEHRLTQAISAGISGAVIVTTADIANST 80
TIR
aC2
bD
aD1
aD2
DE loop
aE
E84*
Y115*
MkeTIR-SAVED 79 VVREVEAPRLLRLHRSSPQFALGIVNAIQTS-TGVVDYDAPDRVLGMERPELRSVDQKSASRLGLVTMARQMLWHRIAAI 157
WP_106298945.1 81 VVKTLEAPQLLELHRDHDVFALGIINSVKTE-DDGTDYDAPDRLLEIRPGTLSGVDQQSAERDGLLALIRGLVWHRIASL 159
WP_114906686.1 81 VVKTLEAPQLLELHRDHEVFALGIINSVKTD-DGGTNYDAPDRLLEIRPGTLSGVDQQSAERDGLLALIRGLVWHRIASL 159
WP_135831082.1 76 VVQHVESPRLIELHSDHPQFVLGIANAVERE-PGKLDYDAPDRVLLKRPGTLNSVDQSPANRAGLINLVGKLVFHRIAAQ 154
WP_028708504.1 78 IVRSIEAPKLIDLHRDDPRFQLLIANDIAKD-TGSPDYTAPDRLLGRVKDDLKGVDQSATSAEELLALTQKALTHRMVQH 156
WP_056712690.1 76 VVQHVESPRLIELHQQHPEFTLGIVNAVERE-PGKIDYTAPERVLLKRQGTLSGVDQTEVSRGGMVGLAKGMVLQRVANR 154
WP_136031783.1 78 IVRGIEAPKLIDLHRSDARFQLLIANDVAKESSASLDYSAPDRLLGRVKDDLKGVDQSGTSPEGLLSLVGKAVAHRMAQH 157
WP_036368247.1 81 VVKFLEAPLLLQIHDDYPEFALAVANAIENE-HGSLDYTAPDKLLGVKPGTLAGVDQHRVDRAELLHIVDRLLRQRVANH 159
K199*
MkeTIR-SAVED 158 RPLLSASGGELRLSLQTRNTPQVYDRTDADLDIRIRPSAHEKLPSAHGLEDFAETAQFLPDAVTRAGANGVRIEGGAHLS 237
WP_106298945.1 160 RKRIEATDQTFHLSLQTRNTPQVYDRTGDELDIRLRPSDHERLPSADGLRDLKDTIGLLPDAVTRSGAHRLRVAGGAHLS 239
WP_114906686.1 160 RKRIEATDQTFHLSLQTRNTPQVYDRTGDELDIRLMPSDHERLPSADGLRDLKDTIGLLPDAVTRSGAHRLRVAGGAHLS 239
WP_135831082.1 155 RELNGTDDT-FNISIQTRNTPQVYDRTGSELDIRIRPNTHERLPSVPGLVDLADVIRFIPGAVTRSSAKRVQVRGGAHLT 233
WP_028708504.1 157 RAAVEANGV-FELTIQTRNVGQVYDRTGAQLDIRVRRSNHEKLPDSAGLEDLRRTLGLLPDAITSTGARKVRVGGGAHLS 235
WP_056712690.1 155 RARGIYEDTPFTISVQTRNTPQVYDRTGADLDIRLQPGSDERLPSPNGLRDLADTVGNLPTAATRAAAQRVRIEGGAHLA 234
WP_136031783.1 158 RPLVENNGR-FDLSIQTRNIGQVYDRTGAQLDIRVRRSSHETLPDSAGLEDLRRSLTLLPDAITRTGARAVRITGGAHLS 236
WP_036368247.1 160 RAHVADTHL-FELSVQTRNAPQSFDRTLGQLDIRLRPAGHGRLPSAAGLSDLRDTIGLLPDAVTQSAAERVRIRGGAHLC 238
SAVED
MkeTIR-SAVED 238 VSIAIGAAIPSTRVGPMTVVDGRGVHWVSSTEPQLPDEPRLRIVRESTIPSTAPAPGRPDVAAYIDLQHPRSDAAFDNYL 317
WP_106298945.1 240 VAFAVGAALPSSRIGHMDVIDQQGATWASDGEARFVTQPQVQIAAQGGDPSAIT-TGRPSVAVYVDLLPQRSDTAFTRYI 318
WP_114906686.1 240 VAFAVGAALPSSRIGHMDVIDQQGATWSSDGEARFITQTQVQIANQGGEPSAIT-TGRPSAAVYVDLLPQRSDTAFTRYI 318
WP_135831082.1 234 VAFALGAAIPSSRVGNLEVVDQRGDSWTSGTEADLSDPALLEVTGSGSNPQLSS-TGRSKVAIYLDLLQRRSDAAYERYL 312
WP_028708504.1 236 VAFALGIALPSSRIGQLEVIDQRSDVWASGPEAAVPTPPTLHF--DVTEHPTVP-GDRPRVAVYVDLLSTQSDAAFERYL 312
WP_056712690.1 235 VAFALGAALPETRVGYIDVTDTFGCTWSSDAGN---SEALVSAESDWTNQT-PP-AGRRTVAVYVDLTAPRSDAAFRRYL 309
WP_136031783.1 237 IAFALGIALPSARIGHLEVVDQRDAIWASGEEAAVPSAPTLQFTATKSEEPAPQ-GTRPTVAVYVDLLPTQSDAAFDRYL 315
WP_036368247.1 239 VAFALGASLPSSRIGHMEVFDQQGSAWSSAGEARFTSPPHIYVERQAINSGVAA-PGRRAVGVYLDLLAQRSDAAFDQYL 317
R388* W394*
MkeTIR-SAVED 318 TEHAAELVAWQHLAPTRTGLLDAADGGTIAAEAVAHIRELSMTNGNAVVHLMVRGPFGLAVLIGRLTNTLRVVAYEWTDS 397
WP_106298945.1 319 EDHRPFLSAWRHLTSASGTLLDPADAGLIAADVAAHIRALSNDNSNAEVHLLLRCPFPLALLIGRLTNTLRVVVHEWDDS 398
WP_114906686.1 319 EDHRPFLAAWRHLTSASGTLLDPTDAGLIAADVAAHIRALSNDNSNAEVHLLLRCPFPLALLIGRLTNTLRVVVHEWDDS 398
WP_135831082.1 313 DEQGDTLTAWRHLRLGTDDLINPDDAGAVAAEAAHHIRELSETNNNAEAHLLLRCPFPIAVLVGRLCNTLRVTTYEWDDT 392
WP_028708504.1 313 DERGETLNAHGVIRSPQRGLLDPANAGAVASEVAGLIRQLSGAHSNASVDLLLAVPFGLAVLIGRLSNTLRVRLFEWDDT 392
WP_056712690.1 310 DEHGSGLAAWAHVVPTQEGRLDPSDAGALAREVADHMRELSAKHDNADVHVLLHCPFGVAVLVGRLTNTLRMTAFEWAPA 389
WP_136031783.1 316 AEHGEELDAYAVIRLHERGLIDPARAGAIASEVAGLIRQLSATYGNAQVDLLLALPFGLAVLIGRLCNTLRLRVFEWDNS 395
WP_036368247.1 318 EANDQDLTAWQHMRSSGGDLLDPSLAGATAADAAAHIRALANDHANADVHLLLRCPFPIAMLMGRLTNTLRVVAYEWDDS 397
MkeTIR-SAVED 398 D-APDG-TFMPPRYEPIVQLRASTPAGVIERVIVADAE 433
WP_106298945.1 399 D-PIDG-EDYRARYVPTLRVRTSASSGVIEDVLLPDAS 434
WP_114906686.1 399 D-PIDG-EDYRARYVPTMRLRTSASSGVIEDVLLPDAS 434
WP_135831082.1 393 D-PAKGDADYRARYVATMKIRPSAATGAIEQVLPTH 427
WP_028708504.1 393 DNPADNSVDVRPRYVACLEARAGSPAGPITSVSLQSCTG 431
WP_056712690.1 390 D-PADG--DHRPRYVPVVDLVTTAPAGVITKVY 419
WP_136031783.1 396 DDEASS--DARPRYVPCVAVRANSSSGPITAVLLEACTA 432
WP_036368247.1 398 DDGIDA--DGRPCYVPALRVRASAATGVIEEVLLRDTRDDRS 437

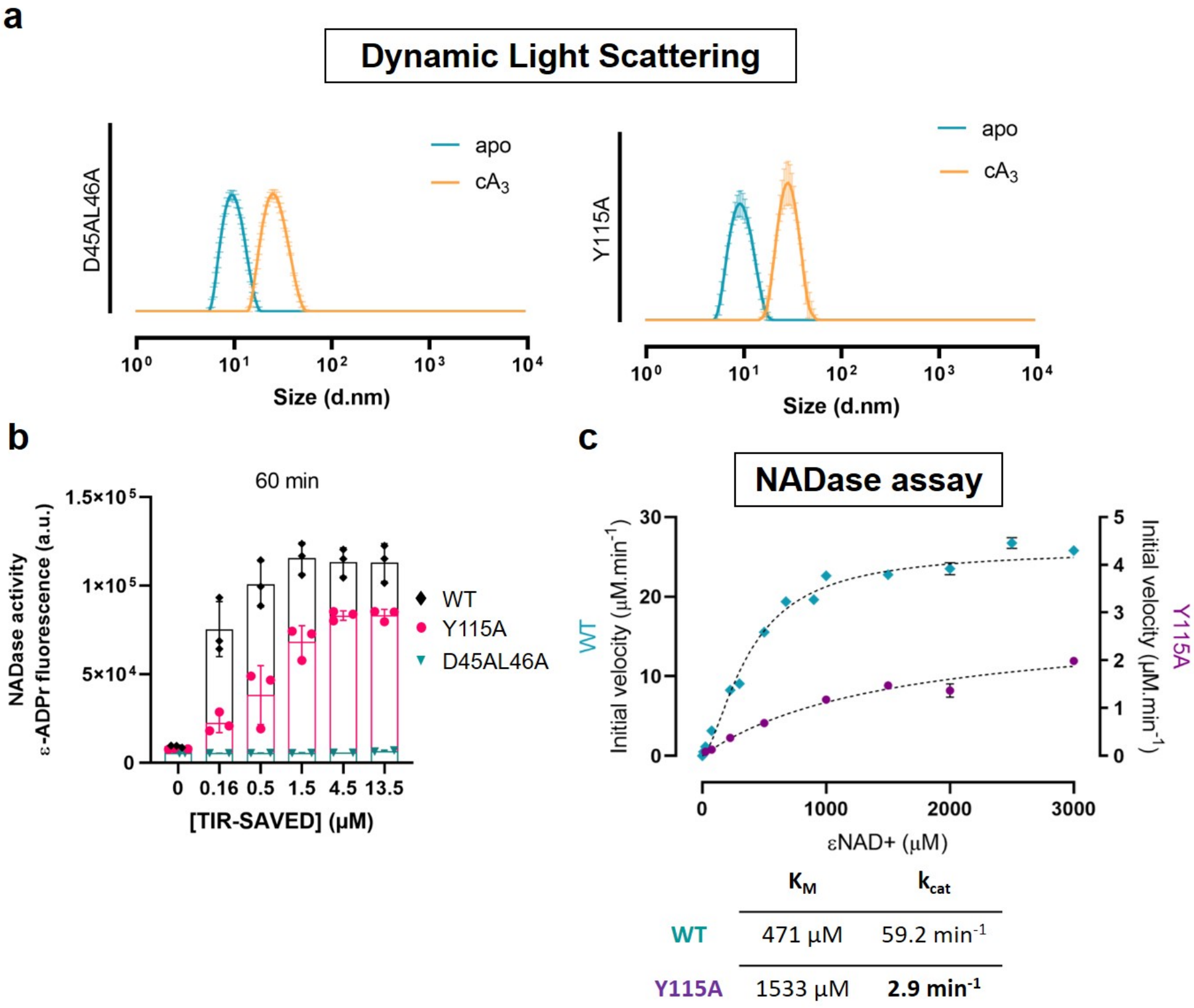
a
Dynamic Light Scattering
D45AL46A
apo
cA3
10^0
10^1
10^2
10^3
10^4
Size (d.nm)
Y115A
apo
cA3
10^0
10^1
10^2
10^3
10^4
Size (d.nm)
b
60 min
NADase activity
ε-ADPr fluorescence (a.u.)
1.5×10^5
1×10^5
5×10^4
0
WT
Y115A
D45AL46A
0
0.16
0.5
1.5
4.5
13.5
[TIR-SAVED] (μM)
c
NADase assay
WT
Initial velocity (μM.min^-1)
30
20
10
0
Y115A
Initial velocity (μM.min^-1)
5
4
3
2
1
0
0
1000
2000
3000
εNAD+ (μM)
K_M
k_cat
WT
471 μM
59.2 min^-1
Y115A
1533 μM
2.9 min^-1

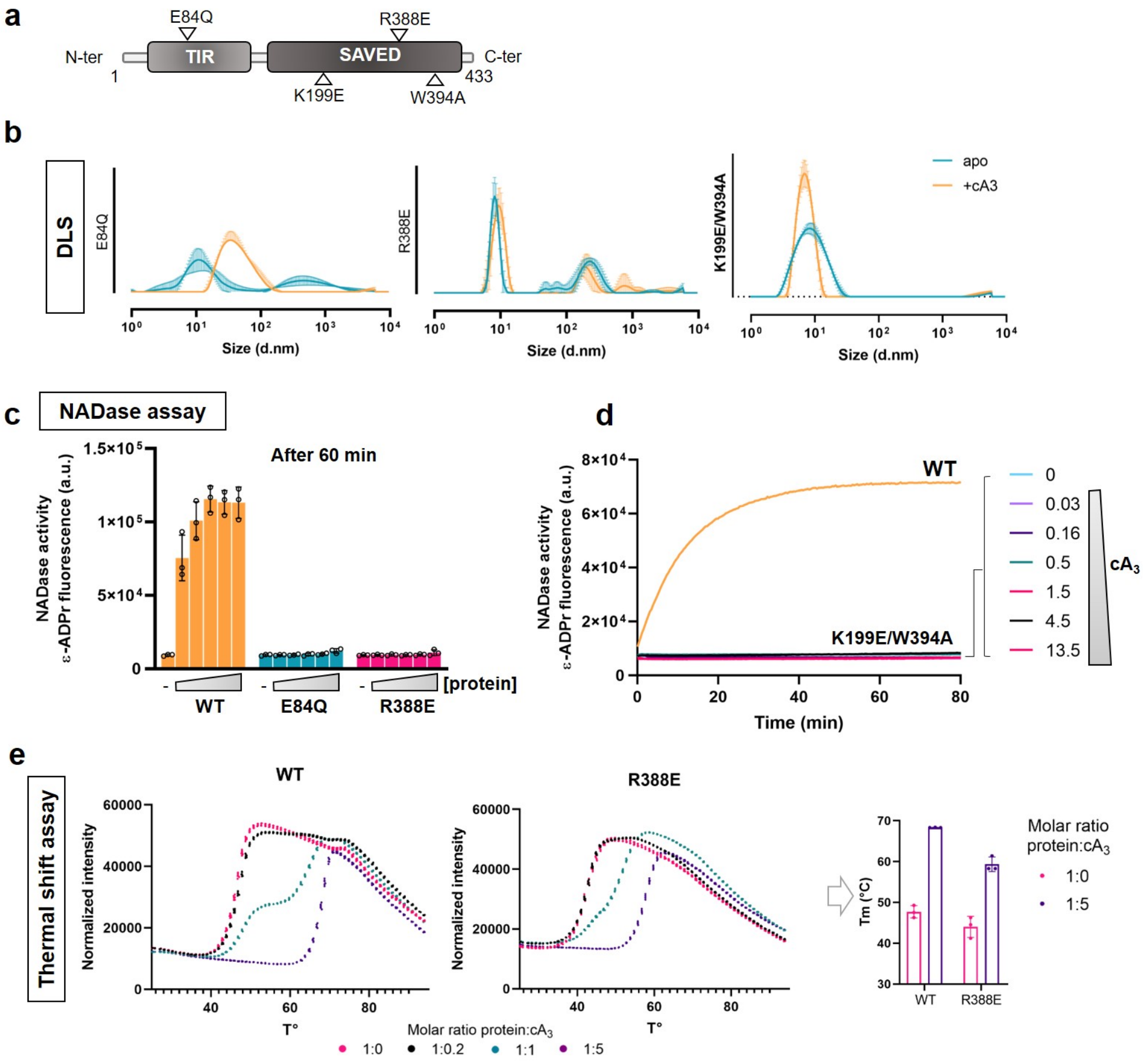
a
E84Q
R388E
N-ter
TIR
SAVED
C-ter
1
433
K199E
W394A
b
DLS
E84Q
R388E
K199E/W394A
apo
+cA3
Size (d.nm)
c
NADase assay
After 60 min
NADase activity
ε-ADPr fluorescence (a.u.)
[protein]
WT
E84Q
R388E
d
WT
K199E/W394A
Time (min)
0
0.03
0.16
0.5
1.5
4.5
13.5
cA3
e
Thermal shift assay
WT
R388E
Normalized intensity
T°
Molar ratio protein:cA3
1:0
1:0.2
1:1
1:5
Tm (°C)
Molar ratio protein:cA3
1:0
1:5

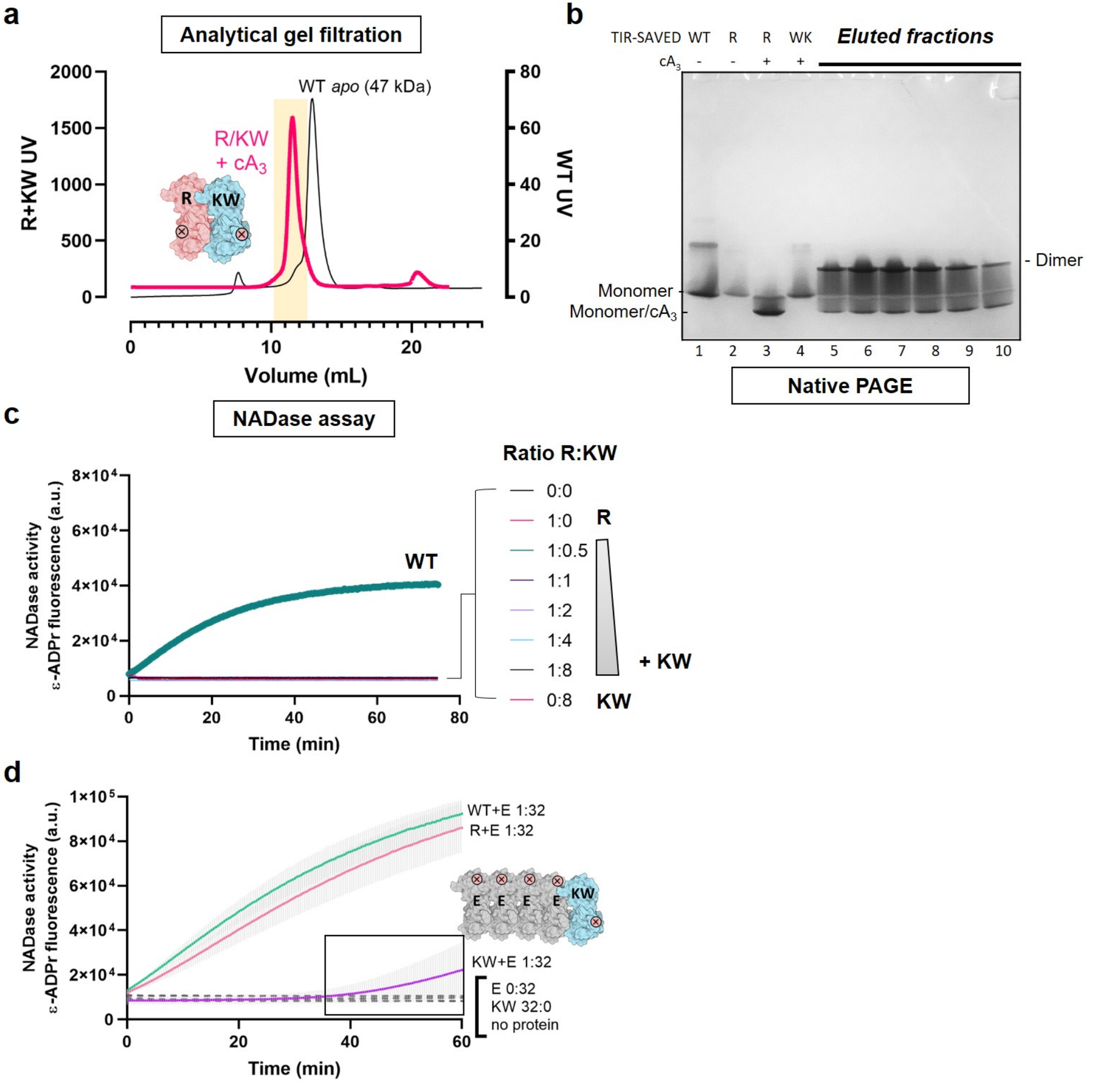
a
Analytical gel filtration
WT apo (47 kDa)
R/KW
+ cA3
R
KW
R+KW UV
WT UV
Volume (mL)
b
TIR-SAVED WT R R WK
cA3 - - + +
Eluted fractions
- Dimer
Monomer
Monomer/cA3
1 2 3 4 5 6 7 8 9 10
Native PAGE
c
NADase assay
Ratio R:KW
0:0
1:0
1:0.5
1:1
1:2
1:4
1:8
0:8
R
+ KW
KW
WT
NADase activity
ε-ADPr fluorescence (a.u.)
Time (min)
d
WT+E 1:32
R+E 1:32
KW+E 1:32
E 0:32
KW 32:0
no protein
E
KW
NADase activity
ε-ADPr fluorescence (a.u.)
Time (min)

	TIR-SAVED/cA$_3$ (EMDB-14122) (PDB 7QQK)
Data collection and processing	
Magnification	60,000x
Voltage (kV)	300
Electron exposure (e–/Å^2)	64.1
Defocus range (μm)	-1.0 to -3.1
Pixel size (Å)	0.997
Symmetry imposed	C1
Initial particle images (no.)	1,228,401
Final particle images (no.)	596,378
Map resolution (Å)	3.84
FSC threshold	0.143
Map resolution range (Å)	2.28-8.16
Refinement	
Initial model used (PDB code)	AF2 (AlphaFold2 model)
Model resolution (Å)	3.84
FSC threshold	0.143
Model resolution range (Å)	
Map sharpening *B* factor (Å^2)	-176.5
Model composition	
Non-hydrogen atoms	26752
Protein residues	1732
Ligands	RNA
B factors (Å^2)	
Protein	42.52/127.78/69.82
Nucleotide	49.53/78.71/61.61
R.m.s. deviations	
Bond lengths (Å)	0.005 (0)
Bond angles (°)	1.092 (0)
Validation	
MolProbity score	2.27
Clashscore	25.90
Poor rotamers (%)	0.29
Ramachandran plot	
Favored (%)	94.61
Allowed (%)	4.99
Disallowed (%)	0.41